A Stochastic Multiscale Model for Microstructure Model Reduction

Bin Wen[a], Nicholas Zabaras[a]

[a] *Materials Process Design and Control Laboratory, Sibley School of Mechanical and Aerospace Engineering, Cornell University, Ithaca, NY 14853-3801, USA*

Abstract

The mechanical properties of a deformed workpiece are sensitive to the initial microstructure. Often, the initial microstructure is random in nature and location specific. To model the variability of properties of the workpiece induced by variability in the initial microstructure, one needs to develop a reduced order stochastic input model for the initial microstructure. The location-dependence of microstructures dramatically increases the dimensionality of the stochastic input and causes the "curse of dimensionality" in a stochastic deformation simulation. To quantify and capture the propagation of uncertainty in multiscale deformation processes, a novel data-driven bi-orthogonal Karhunen-Loève (KL) decomposition strategy is introduced. The multiscale random field representing random microstructures over the workpiece is decomposed simultaneously into a few modes in the macroscale and mesoscale. The macro modes are further expanded through a second-level KL expansion to separate the random and spatial coordinates. The few resulting random variables are mapped to the uniform distribution via a polynomial chaos (PC) expansion. As a result, the stochastic input complexity is remarkably simplified. Sampling from the reduced random space, new microstructure realizations are reconstructed. By collecting the properties of workpieces with randomly sampled microstructures, the property statistics are computed. A high-dimensional multiscale disk forging example of FCC nickel is presented to show the merit of this methodology, and the effect of random initial crystallographic texture

*Corresponding author: N. Zabaras, Fax: 607-255-1222, Email: zabaras@cornell.edu, URL: http://mpdc.mae.cornell.edu/

Report Documentation Page

Form Approved
OMB No. 0704-0188

Public reporting burden for the collection of information is estimated to average 1 hour per response, including the time for reviewing instructions, searching existing data sources, gathering and maintaining the data needed, and completing and reviewing the collection of information. Send comments regarding this burden estimate or any other aspect of this collection of information, including suggestions for reducing this burden, to Washington Headquarters Services, Directorate for Information Operations and Reports, 1215 Jefferson Davis Highway, Suite 1204, Arlington VA 22202-4302. Respondents should be aware that notwithstanding any other provision of law, no person shall be subject to a penalty for failing to comply with a collection of information if it does not display a currently valid OMB control number.

1. REPORT DATE	2. REPORT TYPE	3. DATES COVERED
19 DEC 2011		**00-00-2011 to 00-00-2011**

4. TITLE AND SUBTITLE
A Stochastic Multiscale Model for Microstructure Model Reduction

5a. CONTRACT NUMBER
5b. GRANT NUMBER
5c. PROGRAM ELEMENT NUMBER

6. AUTHOR(S)

5d. PROJECT NUMBER
5e. TASK NUMBER
5f. WORK UNIT NUMBER

7. PERFORMING ORGANIZATION NAME(S) AND ADDRESS(ES)
Cornell University,Sibley School of Mechanical and Aerospace Engineering,Materials Process Design and Control Laboratory,Ithaca,NY,14853

8. PERFORMING ORGANIZATION REPORT NUMBER

9. SPONSORING/MONITORING AGENCY NAME(S) AND ADDRESS(ES)

10. SPONSOR/MONITOR'S ACRONYM(S)
11. SPONSOR/MONITOR'S REPORT NUMBER(S)

12. DISTRIBUTION/AVAILABILITY STATEMENT
Approved for public release; distribution unlimited

13. SUPPLEMENTARY NOTES

14. ABSTRACT
The mechanical properties of a deformed workpiece are sensitive to the initial microstructure. Often, the initial microstructure is random in nature and location specific. To model the variability of properties of the workpiece induced by variability in the initial microstructure, one needs to develop a reduced order stochastic input model for the initial microstructure. The location-dependence of microstructures dramatically increases the dimensionality of the stochastic input and causes the ?curse of dimensionality? in a stochastic deformation simulation. To quantify and capture the propagation of uncertainty in multiscale deformation processes, a novel data-driven bi-orthogonal Karhunen-Lo'eve (KL) decomposition strategy is introduced. The multiscale random field representing random microstructures over the workpiece is decomposed simultaneously into a few modes in the macroscale and mesoscale. The macro modes are further expanded through a second-level KL expansion to separate the random and spatial coordinates. The few resulting random variables are mapped to the uniform distribution via a polynomial chaos (PC) expansion. As a result, the stochastic input complexity is remarkably simplified. Sampling from the reduced random space, new microstructure realizations are reconstructed. By collecting the properties of workpieces with randomly sampled microstructures, the property statistics are computed. A high-dimensional multiscale disk forging example of FCC nickel is presented to show the merit of this methodology, and the effect of random initial crystallographic texture on the macroscopic properties.

15. SUBJECT TERMS
Stochastic multiscale simulation, multiscale model reduction, location-dependent microstructure, bi-orthogonal decomposition, Karhunen-Loeve expansion, polynomial chaos expansion, property variability.

16. SECURITY CLASSIFICATION OF:			17. LIMITATION OF ABSTRACT	18. NUMBER OF PAGES	19a. NAME OF RESPONSIBLE PERSON
a. REPORT **unclassified**	b. ABSTRACT **unclassified**	c. THIS PAGE **unclassified**	**Same as Report (SAR)**	**42**	

Standard Form 298 (Rev. 8-98)
Prescribed by ANSI Std Z39-18

on the macroscopic properties.

Key words: Stochastic multiscale simulation, multiscale model reduction, location-dependent microstructure, bi-orthogonal decomposition, Karhunen-Loève expansion, polynomial chaos expansion, property variability.

---

1. Introduction

For polycrystalline materials (e.g. metals, alloys, etc.), macroscale properties are sensitive to the underlying microstructure. In this work, we are interested in modeling the variability of properties of the workpiece in a deformation process induced by variability in the initial microstructure. To accurately evaluate the properties of a given microstructure at a given material point, homogenization strategy over a statistical volume element (SVE) [1, 2, 3] has been widely applied. In the context of polycrystalline materials, an SVE is a microstructure containing finite number of grains (see Fig. 1) with features (grain and texture distribution) that satisfy certain statistical constraints. Given a number of correlated realizations of the microstructure, a stochastic data-driven model of the microstructure is produced that when coupled with uncertainty quantification methods (e.g. Monte Carlo or sparse grid methods) can be used to compute the distribution of properties at the material point. However, in order to investigate the variability of macroscopic properties in a workpiece due to microstructure randomness, we need to exploit the stochastic space of initial microstructures in the workpiece and not simply at a material point.

Microstructure uncertainty at a material point has been extensively studied using a variety of methods. In [4, 5] the principle of maximum entropy (MaxEnt) was used to describe the microstructure topology of binary and polycrystalline materials. A set of correlation functions or grain size moments were given as the prescribed constraints. Realizations of microstructures were then sampled from such MaxEnt distribution and interrogated using appropriate physical model, e.g. a crystal plasticity finite element method (CPFEM) [6] for polycrystals. The Monte Carlo (MC) method was adopted to find the error-bars of effective stress-strain response of FCC aluminum. In [7], the orientation distribution function (ODF) was adopted to describe the polycrystalline mi-

crostructure. A number of ODF samples were given as the input data. Karhunen-Loève expansion (KLE) [8, 9] was utilized to reduce the input complexity and facilitate the high-dimensional stochastic simulation. An adaptive version of sparse grid collocation strategy [10, 11] was used to find the stress-strain curve with error bars and the convex hull of elastic modulus of FCC aluminum after deformation. Mechanical response variability and thermal properties due to both orientation and grain size uncertainties were studied in [12, 13]. A nonlinear model reduction technique based on manifold learning [14] has been introduced to find the surrogate space of the grain size feature while grain orientations were reduced by KLE. Critical stress distribution after deformation was constructed for FCC nickel [12] and effective thermal conductivity distribution was explored for crystals with ortho-symmetry [13]. Recently, variability of fatigue resistance, measured by strain-based fatigue indicator parameters (FIPs) [15] of two-phase nickel-based superalloys was studied with the assistance of principal component analysis (PCA) [16]. Distributions of FIPs, as well as their convex hulls showing the extreme values, of microstructures sharing identical statistical features with given samples under cyclic loading were extracted. Convergence with increasing dimensionality of the reduced-order representation was also shown.

To quantify the effect of microstructures on macro-properties and probe the uncertainty propagation through different length scales, a multiscale simulator needs to be adopted. Each point of the workpiece is associated with a microstructure in the mesoscale, the deformation of which is controlled by the local deformation gradient estimated in the macroscale. Mechanical properties/response of the point are evaluated via proper (e.g. crystal plasticity) constitutive model applied on the deformed microstructure. Since microstructures are random, properties of the workpiece are also random. In general, microstructures are location-specific (meaning that microstructures associated with different spatial points may have different distributions) [17]. As a result, the stochastic input to the probabilistic multiscale forging simulation will be extremely high dimensional, which prevents one from quantifying the uncertainties of interested properties. This problem is usually referred to as the “curse of dimensionality”. Conventional model reduction schemes that only locally decompose input complexity within a single scale and cannot see the correlation between macroscale points

are not sufficient for reducing the multiscale stochastic input. To this end, we introduced a bi-orthogonal KLE strategy [18, 19], which decomposes the multiscale random field into a few modes in both the macro- and meso-scales [20]. Mean and standard deviation of elastic moduli, i.e. Young's modulus, shear modulus, and bulk modulus, over the product were investigated given texture (orientation distribution) uncertainty of FCC copper microstructures. However, this earlier work limited its stochastic input to two prescribed random variables. In this work, we will build the bi-orthogonal KLE on the basis of a given set of microstructure data. Different types of macroscale inner products are discussed. A second-level KLE is conducted to further reduce the dimensionality of the stochastic space after bi-orthogonal decomposition. The optimal dimensionality of the final reduced-order space will be determined based on the energy proportion captured by the principal components in the two-step decomposition. A non-intrusive strategy is used to project the reduced random variables to the space of random variables with known probability distributions. Low order statistics of equivalent stress, strain, and strength fields of disks after forging are studied by repeatedly calling the deterministic solver using microstructures sampled in the reduced space. We use Monte Carlo (MC) sampling to construct the stochastic solution.

The rest of the paper is organized as follows. In Section 2, the representation of microstructure and the multiscale forging simulator are introduced. Theory and formulation of the bi-orthogonal KL decomposition, followed by a second-level KLE to further decompose the resulting spatial-random coupled modes, will be enunciated in Section 3. The reduced microstructure representations are mapped to a multi-dimensional uniform distribution via polynomial chaos expansion (PCE) so that sampling of microstructures becomes efficient. The detail of this procedure is presented in Section 4. Problem definition and generation of initial samples are described in Section 5. Section 6 shows an example of stochastic multiscale modeling of nickel disk forging. Properties/response variability of the product will be investigated. Finally, conclusions and discussion are given in Section 7.

2. Multiscale Modeling of a Forging Process

To study the variability of mechanical properties induced by microstructure uncertainty in forging disks, a multiscale framework which couples finite element (FE) large deformation simulator with crystal plasticity constitutive model is introduced as the deterministic solver. Each point in the macroscale is linked to a mesoscale polycrystalline microstructure described by its grain size and orientation features. The mechanical properties and response of the material under deformation are evaluated in the microstructure domain and returned to the workpiece.

2.1. Multiscale Forging Solver

An updated Lagrangian implicit FE model for the analysis of large deformation forging processes is employed for the multiscale simulation. This model, seamlessly integrating kinematic, contact, and constitutive modules, is suitable for forging problem of any material subjected to various die shapes. A crystal plasticity model is used in this work. Each point (effectively, Gauss integration point) of the macroscale workpiece is represented by a polycrystalline microstructure whose deformation is controlled by the local deformation gradient $\mathbf{F}$, while the mechanical properties/response (e.g. effective stress, strain, strength, etc.) at that point are evaluated in the mesoscale and returned to the workpiece after homogenization [21]. The multiscale framework is summarized below.

Macroscale: Let $\mathbf{X}$ be a material particle in the initial configuration $\mathcal{B}_0$ and $\mathbf{x} = \mathbf{x}(\mathbf{X}, t_{n+1})$ be its location at time t_{n+1}. The total deformation gradient defined as

$$\mathbf{F}(\mathbf{X}, t_{n+1}) = \nabla_0 \mathbf{x}(\mathbf{X}, t_{n+1}) = \frac{\partial \mathbf{x}(\mathbf{X}, t_{n+1})}{\partial \mathbf{X}}, \tag{1}$$

can be expressed as the product of $\mathbf{F}_n$ at the previous time step $t = t_n$ and the relative deformation gradient $\mathbf{F}_r$:

$$\mathbf{F} = \mathbf{F}_r \mathbf{F}_n. \tag{2}$$

The equilibrium equation at $t = t_{n+1}$ is expressed in the reference configuration $\mathcal{B}_n$ as

$$\nabla_n \cdot \langle \mathbf{P}_r \rangle_h + \mathbf{f}_r = 0, \tag{3}$$

where ∇_n denotes the divergence in $\mathcal{B}_n$. $\mathbf{f}_r$ can be represented as

$$\mathbf{f}_r = \det \mathbf{F}_r \mathbf{b}, \tag{4}$$

where $\mathbf{b}$ is the body force defined on the current configuration. The material behavior is obtained from the deformation of the microstructure through homogenization. The function $\langle \cdot \rangle_h$ denotes the homogenized property over the microstructure. Therefore, $\langle \mathbf{P}_r \rangle_h$ is the homogenized first Piola-Kirchhoff (PK) stress expressed per unit area of $\mathcal{B}_n$ and given as:

$$\langle \mathbf{P}_r \rangle_h = \langle \det \mathbf{F}_r^s \mathbf{T} \mathbf{F}_r^{s-T} \rangle_h = \det \mathbf{F}_r \langle \mathbf{T} \rangle_h \mathbf{F}_r^{-T}, \tag{5}$$

where $\mathbf{F}_r^s$ is the mesoscale relative deformation gradient, which equals the macroscopic $\mathbf{F}_r$ under Taylor hypothesis for macro-meso linking. $\langle \mathbf{T} \rangle_h$ is the homogenized Cauchy stress defined as the volume average of the mesoscale stress $\mathbf{T}$:

$$\langle \mathbf{T} \rangle_h = \bar{\mathbf{T}} = \frac{1}{V} \int_{\mathcal{B}_{n+1}} \mathbf{T} dV. \tag{6}$$

An incremental quasi-static problem is solved to determine the displacement field $\mathbf{u}(\mathbf{x}_n, t_{n+1})$ that satisfies Eq. (3) and boundary conditions. The solution of the deformation problem proceeds incrementally in time starting from the initial configuration $\mathcal{B}_0$. The weak form of the governing equation in the presence of die contact can be written as:

$$\tilde{G}(\mathbf{u}_{n+1}, \tilde{\mathbf{u}}) \equiv \tilde{G}_b(\mathbf{u}_{n+1}, \tilde{\mathbf{u}}) + \tilde{G}_c(\mathbf{u}_{n+1}, \tilde{\mathbf{u}}) = 0, \tag{7}$$

where the first term is the virtual work of the workpiece:

$$\begin{aligned} \tilde{G}_b(\mathbf{u}_{n+1}, \tilde{\mathbf{u}}) &= \int_{\mathcal{B}_n} \langle \mathbf{P} \rangle_h \cdot \frac{\partial \tilde{\mathbf{u}}}{\partial \mathbf{x}_n} dV \\ &- \left(\int_{\partial \mathcal{B}_{n+1}} \bar{\mathbf{t}} \cdot \tilde{\mathbf{u}} dS + \int_{\mathcal{B}_{n+1}} \bar{\mathbf{b}} \cdot \tilde{\mathbf{u}} dV \right), \end{aligned} \tag{8}$$

and the second term is the contact virtual work:

$$\tilde{G}_c(\mathbf{u}_{n+1}, \tilde{\mathbf{u}}) = \int_{\partial \mathcal{B}_n^c} (-\bar{\mathbf{t}}_{cN} \cdot \tilde{\mathbf{u}} + \bar{\mathbf{t}}_{cT} \cdot \tilde{\mathbf{u}}) dS, \tag{9}$$

where $\tilde{\mathbf{u}}$ is the virtual displacement; $\bar{\mathbf{t}}$ is the traction and $\bar{\mathbf{b}}$ is the body force of the bulk; $\partial \mathcal{B}_n^c \subset \partial \mathcal{B}_n$ is the surface corresponding to regions of the body that may potentially

come into contact with the die. $\bar{\mathbf{t}}_{cN}$ and $\bar{\mathbf{t}}_{cT}$ are the normal and tangential tractions at the die due to contact (and friction). The contact work is calculated in the reference configuration $\mathcal{B}_n$. Newton-Raphson iterative scheme along with a line search method is used to solve this non-linear system. The linearization of the weak form at the $(k+1)$-th iteration becomes

$$\tilde{G}(\mathbf{u}_{n+1}^{(k)}, \tilde{\mathbf{u}}) + \frac{\partial \tilde{G}}{\partial \mathbf{u}_{n+1}^{(k)}}(\mathbf{u}_{n+1}^{(k+1)} - \mathbf{u}_{n+1}^{(k)}) = 0. \tag{10}$$

The increment of internal work $\tilde{G}_b$ is computed by

$$d\tilde{G}_b = \int_{\mathcal{B}_n} d\langle \mathbf{P}_r \rangle_h \cdot \frac{\partial \tilde{\mathbf{u}}}{\partial \mathbf{x}_n} dV. \tag{11}$$

The linearization of the homogenized PK-I stress is

$$\begin{aligned} d\langle \mathbf{P}_r \rangle_h &= \det \mathbf{F}_r \Big(tr(d\mathbf{F}_r \mathbf{F}_r^{-1}) \langle \mathbf{T} \rangle_h \\ &- \langle \mathbf{T} \rangle_h (d\mathbf{F}_r \mathbf{F}_r^{-1})^T + \langle d\mathbf{T} \rangle_h \Big) \mathbf{F}_r^{-T}. \end{aligned} \tag{12}$$

The homogenized Cauchy stress $\langle \mathbf{T} \rangle_h$ and its gradient with respect to $d\mathbf{F}_r$ are evaluated using the constitutive model in the mesoscale.

Mesoscale: As mentioned earlier, each Gauss point of the workpiece in the macroscale corresponds to a polycrystalline microstructure, which is described by the sizes and orientations of its constituent grains. According to the Taylor hypothesis, all grains of the same microstructure are subject to the same deformation gradient $\mathbf{F}$, which is identical to the local deformation gradient at that point of the workpiece. The mechanical response of each grain is computed using the crystal plasticity constitutive model [6, 22] and averaged over the microstructure to represent the corresponding quantity in the macroscale. In this paper, we are interested in FCC nickel polycrystals. For details of the constitutive model, the reader is referred to [23]. We here only briefly review the main algorithm.

The total deformation gradient $\mathbf{F}$ is multiplicatively decomposed into elastic and plastic parts

$$\mathbf{F} = \mathbf{F}^e \mathbf{F}^p, \tag{13}$$

where $\mathbf{F}^e$ is the elastic deformation gradient and $\mathbf{F}^p$ is the plastic counterpart with

$\det \mathbf{F}^p$ being 1. The PK-II stress is computed by

$$\hat{\mathbf{T}} = \mathcal{L}^e \mathbf{E}^e = \frac{1}{2}\mathcal{L}^e(\mathbf{F}^{eT}\mathbf{F}^e - \mathbf{I}), \tag{14}$$

where $\mathcal{L}^e$ is the fourth-order elasticity tensor represented in the sample coordinate system and $\mathbf{I}$ is the second-order identity tensor.

The resolved shear stress $\tau^{(\alpha)}$ on slip system α is calculated as

$$\tau^{(\alpha)} = \hat{\mathbf{T}} : \mathbf{S}^{(\alpha)}, \tag{15}$$

where $\mathbf{S}^{(\alpha)} \equiv \mathbf{m}^{(\alpha)} \otimes \mathbf{n}^{(\alpha)}$ is the Schmid tensor defined by the tensor product of the slip direction $\mathbf{m}^{(\alpha)}$ and slip normal $\mathbf{n}^{(\alpha)}$ of slip system α. If $|\tau^{(\alpha)}|$ is larger than the slip resistance $\kappa^{(\alpha)}$, plastic flow on the α-th slip system occurs. The incremental plastic shear strain $\Delta\gamma^{(\alpha)}$ is therefore obtained according to flow rule and utilized to update the slip resistance, deformation gradient, etc. The Taylor strain hardening law based on dislocation density ρ is adopted for the homogeneous evolution of slip resistance κ.

$$\kappa = \kappa_0 + \alpha_t \mu b \sqrt{\rho}, \tag{16}$$

where

$$\dot{\rho} = \sum_{\alpha} \left(\frac{1}{L_g b} + k_1 \sqrt{\rho} - k_2 \rho \right) |\dot{\gamma}^{(\alpha)}|, \tag{17}$$

and α_t is a constant representing an average of the junction strength over all existing dislocation configurations, μ is the shear strength, and b is the magnitude of the Burgers vector. The first term in Eq. (17) represents a geometric storage due to lattice incompatibility, describing the grain boundary hardening. L_g is the grain size parameter [12, 24]. The second term describes storage through a statistical measure of forest dislocation, describing the dislocation interaction hardening inside grains. The last term represents a dynamic recovery rate that renders dislocation segments inactive as they rearrange themselves [22]. The parameters k_1 and k_2 are given as

$$k_1 = \frac{2\theta_0}{\alpha_t \mu b}, \quad k_2 = \frac{2\theta_0}{\kappa_s - \kappa_0}, \tag{18}$$

where θ_0 is the initial hardening rate, κ_0 and κ_s are the initial yield stress and saturation strength, respectively. Substituting Eqs. (17) and (18) into Eq. (16), we can derive at

the hardening rate as

$$\dot{\kappa} = \left\{ \frac{\alpha_t^2 \mu^2 b}{2L_g(\kappa - \kappa_0)} + \theta_0 \left(\frac{\kappa_s - \kappa}{\kappa_s - \kappa_0} \right) \right\} \sum_{\alpha} |\dot{\gamma}^{(\alpha)}|. \tag{19}$$

Therefore, the slip resistance at $t = t_{n+1}$ is updated as

$$\kappa_{n+1} = \kappa_n + \dot{\kappa} \Delta\, t. \tag{20}$$

An iterative algorithm is designed to solve this system of nonlinear equations. Macroscopic quantities, such as stress and strain, are computed as the volume-average of the mesoscale values over all grains (e.g. Eq. (6)). The macroscopic von-Mises equivalent stress and equivalent strain are calculated in the form of

$$\bar{\sigma}_{eff} = \sqrt{\frac{3}{2} \bar{\mathbf{T}}' \cdot \bar{\mathbf{T}}'}, \tag{21}$$

where $\bar{\mathbf{T}}'$ is the deviatoric part of the homogenized Cauchy stress $\bar{\mathbf{T}}$, and

$$\bar{\varepsilon}_{eff} = \int_0^t \sqrt{\frac{2}{3} \bar{\mathbf{D}} \cdot \bar{\mathbf{D}}} dt, \tag{22}$$

in which $\bar{\mathbf{D}}$ is the average rate of deformation. Grain orientations evolve accordingly due to elastic deformation:

$$\begin{aligned} \mathbf{m}^{(\alpha)} &= \mathbf{F}^e \mathbf{m}_0^{(\alpha)}, \\ \mathbf{n}^{(\alpha)} &= \mathbf{F}^{e-T} \mathbf{n}_0^{(\alpha)}. \end{aligned} \tag{23}$$

The equivalent strength is evaluated as the average slip resistance of all slip systems of all grains in the microstructure:

$$\bar{\kappa}_{eff} = \left\langle \frac{1}{n_{slip}} \sum_{\alpha}^{n_{slip}} \kappa^{(\alpha)} \right\rangle_h. \tag{24}$$

The homogenized properties and response are returned to the macroscale for updating the deformation and response fields of the workpiece. The verification of this particular crystal plasticity constitutive model is discussed in [12].

2.2. Microstructure Representation

In the current work, the Taylor hypothesis is adopted for the macro-mesoscale linking. Accordingly, a microstructure (Fig. 1(a)) can be simply described by an array of topological and orientational features of constituent grains (Fig. 1(b)). For a

microstructure (e.g. FCC nickel) composed of M grains, the first M components of the feature array are sizes of individual grains sorted in ascending order and the rest $3M$ components are the corresponding orientations described by Rodrigues parameters [25], an axis-angle representation that consists of three components defined in Eq. (25):

$$\mathbf{r} = \mathbf{w} \tan \frac{\theta}{2}, \tag{25}$$

where $\mathbf{r} = \{r_1, r_2, r_3\}$ are the three Rodrigues components; $\mathbf{w} = \{w_1, w_2, w_3\}$ gives the direction cosines of the rotation axis with respect to microstructure coordinates; and θ is the rotation angle.

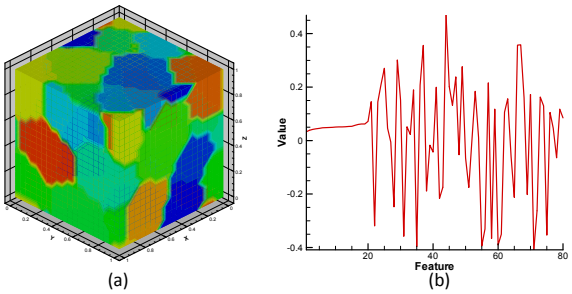

Figure 1: (a) A 3D polycrystalline microstructure with 20 grains. (b) The descriptor of the microstructure. The first 20 components are the sizes of grains, and the last 60 components are the Rodrigues parameters representing grain orientations.

The polycrystalline microstructure is usually a high-dimensional random field, which makes the stochastic simulation intractable. For example, a 20-dimensional vector is needed to store the grain size feature of a microstructure containing 20 grains. The vector will end up to be 80-dimensional when Rodrigues parametrization orientations are considered as well. The situation is even worse when the random field is also a function of spatial location $\mathbf{x}$. If the correlation between microstructures at different points on macroscale is not explored, the dimensionality of the random field explodes. For a random 2D workpiece discretized by n_{el} quadrilateral elements each of which has n_{int} Gauss points, the total dimensionality of the microstructure descriptor ends up to be $4Mn_{el}n_{int}$, where M is the number of grains in the microstructure. In the current work, we assume the random source is only the grain orientations while the grain sizes

are fixed. The total dimensionality of the microstructure stochastic space is therefore $3Mn_{el}n_{int}$, which is still very large. This is referred to as the "curse of dimensionality". A reduced-order surrogate microstructure model of the location dependent random microstructure is needed. By sampling from the low-dimensional surrogate space, uncertainty quantification of the product properties driven by random microstructures becomes computationally feasible.

3. Two-Step Karhunen-Loève Decomposition of the Multiscale Random Microstructure Field

In our previous works on quantifying uncertainties in materials, a set of linear and non-linear model reduction techniques were developed to facilitate the solution of stochastic partial differential equations (SPDEs) describing physical processes in random media [14, 26, 27, 28]. These methods have been successfully applied to reduce the dimensionality of random microstructures at a given material point. However, these techniques cannot be applied to location-dependent microstructures (Fig. 2), e.g. reducing a random microstructure field of the form $\mathbf{A}(\mathbf{x}, \mathbf{s}, \omega)$, where $\mathbf{s}$ is a mesoscale coordinate and $\mathbf{x}$ the macroscopic coordinates. A bi-orthogonal decomposition based on KL expansion was introduced to address this problem in [20]. This algorithm was originally developed for temporal-spatial coupled problems [18], in which the random field , $\mathbf{A}(\mathbf{x}, t, \omega)$, is a function of both time t and spatial coordinates $\mathbf{x}$. Following certain modification, we have applied this idea to multiscale forging problem in [20]. In the current work, we rebuild the bi-orthogonal KLE strictly on the basis of given data and generalize the model to the scenario that the information of the inherent controlling random variables is not known beforehand. The stochastic random field $\mathbf{A}(\mathbf{x}, \mathbf{s}, \omega)$ is decomposed to a set of mesoscale modes $\Psi(\mathbf{s})$ and macro (or spatial)-random coupled modes $\mathbf{\Phi}(\mathbf{x}, \omega)$. A second-level KLE is introduced to further separate random variables ω from the macroscale (spatial) modes. The optimal dimensionality of the reduced-order space will be determined based on the number of principal components preserved in the two-step KLE. Different selections of the inner product in the macroscale are discussed to determine which one is more appropriate for this problem. The algorithm of

bi-orthogonal decomposition (BOD) is summarized below.

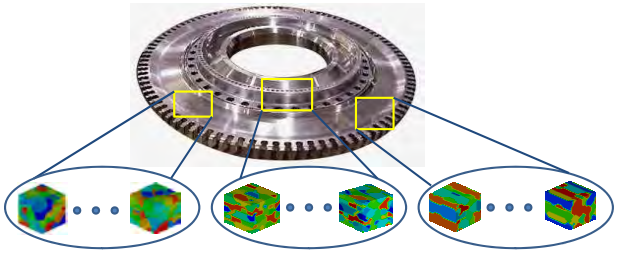

Figure 2: Microstructure dependence on spatial location. At different locations, the microstructures may have different features due to preprocessing.

3.1. Bi-Orthogonal Karhunen-Loève Decomposition

Assume a random field $\mathbf{A}$ defined on a probability space (Ω, F, p)

$$\mathbf{A}(\mathbf{x}, \mathbf{s}, \omega) : \mathcal{S} \times \mathcal{M} \times \Omega \to \mathbb{R}, \tag{26}$$

where $\mathcal{S}$ is the macroscale spatial domain, $\mathcal{M}$ is the microstructure space, Ω is the set of elementary events and $\omega \in \Omega$ is a random field that determines the uncertainty of $\mathbf{A}$ (we call it controlling random variable). $\mathbf{A} = \{A^i, i = 1, \ldots, m\}$ can be the combination of m independent features, e.g., grain size, texture, etc., for describing a microstructure. In the example shown later, m is chosen to be 1 as crystallographic texture is the only random source. The formulation presented in this section takes the general situation where $\mathbf{A}$ is the combination of various features. One can use the idea of Karhunen-Loève expansion to project this field to a set of bi-orthogonal bases in the form of

$$\begin{aligned} \mathbf{A}(\mathbf{x}, \mathbf{s}, \omega) &= \bar{\mathbf{A}}(\mathbf{x}, \mathbf{s}) + \hat{\mathbf{A}}(\mathbf{x}, \mathbf{s}, \omega) \\ &= \bar{\mathbf{A}}(\mathbf{x}, \mathbf{s}) + \sum_{i=1}^{\infty} \sqrt{\rho_i^{(h)}} \Psi_i^{(h)}(\mathbf{s}) \mathbf{\Phi}_i^{(h)}(\mathbf{x}, \omega), \end{aligned} \tag{27}$$

in which $\rho_i^{(h)}$ are eigenvalues of the eigenvalue problem to be defined later on, $\Psi_i^{(h)}$ are mesoscale modes strongly orthogonal in the meso-space, and $\mathbf{\Phi}_i = \{\Phi_i^{(h),1}, \ldots \Phi_i^{(h),m}\}$ are spatial modes weakly orthogonal in macro-space for all the m features. The superscript $(h) = 1, 2, 3$ denotes that we can construct the above expansion according to

certain type of inner products in the macroscale. $\bar{\mathbf{A}}$ is the mean field defined by

$$\bar{\mathbf{A}} = \langle \mathbf{A} \rangle := \int_{\Omega} \mathbf{A}(\mathbf{x}, \mathbf{s}, \boldsymbol{\omega}) p(\boldsymbol{\omega}) d\boldsymbol{\omega}, \tag{28}$$

where $p(\boldsymbol{\omega})$ is the multivariate joint probability density of $\boldsymbol{\omega}$. The definition of $\bar{\mathbf{A}}$ is not unique. For example, in [19], this mean field is also averaged over the temporal domain (analogous to the mesoscale space in the current setup), leaving $\bar{\mathbf{A}}$ a function of spatial coordinates: $\bar{\mathbf{A}} = \bar{\mathbf{A}}(\mathbf{x})$. We here do not average it over the meso domain to be consistent with the previous work [20]. In practice, the random field $\mathbf{A}(\mathbf{x}, \mathbf{s}, \boldsymbol{\omega})$ is usually given by N realizations $\{\mathbf{A}_i(\mathbf{x}, \mathbf{s}, \boldsymbol{\omega}_i)\}_{i=1}^{N}$. As a consequence, the mean field is computed as the average of all given samples. For model reduction, the sum in Eq. (27) is usually approximated by the first finite number of, say d, principal components (modes) that capture most of the energy.

We denote by $(,)$ the inner product in the microstructure domain and by $\{,\}_h$ ($h = 1, 2,$ or 3) different types of inner products in the spatial domain [19], respectively, and obtain

$$(\Psi_i^{(h)}, \Psi_j^{(h)}) := \int_{\mathcal{M}} \Psi_i^{(h)}(\mathbf{s}) \Psi_j^{(h)}(\mathbf{s}) d\mathbf{s}, \tag{29}$$

and

$$\begin{aligned} \{\boldsymbol{\Phi}_i^{(h)}, \boldsymbol{\Phi}_j^{(h)}\}_0 &:= \int_{\mathcal{S}} \langle \boldsymbol{\Phi}_i^{(h)} \rangle \cdot \langle \boldsymbol{\Phi}_j^{(h)} \rangle d\mathbf{x}, \\ \{\boldsymbol{\Phi}_i^{(h)}, \boldsymbol{\Phi}_j^{(h)}\}_1 &:= \int_{\mathcal{S}} \langle \boldsymbol{\Phi}_i^{(h)} \cdot \boldsymbol{\Phi}_j^{(h)} \rangle d\mathbf{x}, \\ \{\boldsymbol{\Phi}_i^{(h)}, \boldsymbol{\Phi}_j^{(h)}\}_2 &:= \int_{\mathcal{S}} \left(\langle \boldsymbol{\Phi}_i^{(h)} \cdot \boldsymbol{\Phi}_j^{(h)} \rangle - \langle \boldsymbol{\Phi}_i^{(h)} \rangle \cdot \langle \boldsymbol{\Phi}_j^{(h)} \rangle \right) d\mathbf{x}. \end{aligned} \tag{30}$$

In this work, the microstructure features are given in the form of discrete vectors (i.e. grain orientations) and the mesoscale coordinates can be considered as the indices of the vector components. Therefore, the inner product in the mesoscale is effectively computed by the dot product of the two vectors. The orthogonality requirements for $\Psi_i^{(h)}$ and $\boldsymbol{\Phi}_i^{(h)}$ are

$$(\Psi_i^{(h)}, \Psi_j^{(h)}) = \delta_{ij}, \tag{31}$$

and

$$\{\boldsymbol{\Phi}_i^{(h)}, \boldsymbol{\Phi}_j^{(h)}\}_h = \delta_{ij}. \tag{32}$$

The mesoscale modes $\Psi_i^{(h)}$ are strongly orthogonal to each other and the macroscale modes $\mathbf{\Phi}_i^{(h)}$ are weakly, in an average sense, orthogonal.

By minimizing the distance (based on the norm defined in Eq. (30)) between the Karhunen-Loève expansion and the original random field, one ends up with

$$\Psi_i^{(h)}(\mathbf{s}) = \frac{1}{\sqrt{\rho_i^{(h)}}}\{\hat{\mathbf{A}}, \mathbf{\Phi}_i^{(h)}\}_h, \tag{33}$$

and from the orthogonality condition, we obtain

$$\mathbf{\Phi}_i^{(h)}(\mathbf{x}, \omega) = \frac{1}{\sqrt{\rho_i^{(h)}}} \int_{\mathcal{M}} \hat{\mathbf{A}}(\mathbf{x}, \mathbf{s}, \omega)\Psi_i^{(h)}(\mathbf{s})d\mathbf{s}. \tag{34}$$

These last two Eqs. (33) and (34) lead to the following eigenvalue problem

$$\rho_i^{(h)}\Psi_i^{(h)}(\mathbf{s}) = \int_{\mathcal{M}} \mathbf{C}^{(h)}(\mathbf{s}, \acute{\mathbf{s}})\Psi_i^{(h)}(\acute{\mathbf{s}})d\acute{\mathbf{s}}, \tag{35}$$

where the covariance matrix $\mathbf{C}^{(h)}$ is

$$\mathbf{C}^{(h)}(\mathbf{s}, \acute{\mathbf{s}}) = \{\hat{\mathbf{A}}(\mathbf{x}, \mathbf{s}, \omega), \hat{\mathbf{A}}(\mathbf{x}, \acute{\mathbf{s}}, \omega)\}_h. \tag{36}$$

In discrete form, the covariance can be written as

$$\begin{aligned}
\mathbf{C}^{(0)}(\mathbf{s}, \acute{\mathbf{s}}) &= \sum_{i_n=1}^{n_{el}} \sum_{i_m=1}^{n_{int}} \left(\frac{1}{N} \sum_{j=1}^{N} \hat{\mathbf{A}}_j(\mathbf{x}_{i_m}^{i_n}, \mathbf{s}) \right) \cdot \\
&\quad \left(\frac{1}{N} \sum_{j=1}^{N} \hat{\mathbf{A}}_j^T(\mathbf{x}_{i_m}^{i_n}, \acute{\mathbf{s}}) \right) \hat{W}_{i_m} |J_{i_n}|, \\
\mathbf{C}^{(1)}(\mathbf{s}, \acute{\mathbf{s}}) &= \frac{1}{N} \sum_{j=1}^{N} \sum_{i_n=1}^{n_{el}} \sum_{i_m=1}^{n_{int}} \hat{\mathbf{A}}_j(\mathbf{x}_{i_m}^{i_n}, \mathbf{s}) \hat{\mathbf{A}}_j^T(\mathbf{x}_{i_m}^{i_n}, \acute{\mathbf{s}}) \hat{W}_{i_m} |J_{i_n}|, \\
\mathbf{C}^{(2)}(\mathbf{s}, \acute{\mathbf{s}}) &= \mathbf{C}^{(1)}(\mathbf{s}, \acute{\mathbf{s}}) - \mathbf{C}^{(0)}(\mathbf{s}, \acute{\mathbf{s}}),
\end{aligned} \tag{37}$$

for different definition of macroscale inner products. In these equations, N is the number of realizations, n_{el} is the number of elements in macroscale (when a FEM discretization of the domain is created), n_{int} is the number of integration points in each element, $|J_{i_n}|$ is the Jacobian determinant of the element i_n, $\hat{W}_{i_m}$ is the integration weight associated with the integration point i_m and $\hat{\mathbf{A}}$ is a matrix containing microstructural features corresponding to integration points, and $\mathbf{x}_{i_m}^{i_n}$ represents global coordinates of the integration point i_m of element i_n in the macroscale.

The three types of covariance matrix defined in Eq. (37) (or equivalently, the inner products in the macroscale Eq. (30)) lead to constructions of different expansions Eq. (27) according to different optimization of the random field $\hat{\mathbf{A}}$: through $h = 0$, we minimize the mean error; through $h = 1$, we minimize the second-order moment of the error (the Euclidian distance between the KL expansion and the random field); and through $h = 2$, we minimize the standard deviation error. The discussion of the three types will be further enunciated later with a practical example.

3.2. A Second-Level KLE

With the bi-orthogonal KL expansion, we decompose the random field $\mathbf{A}(\mathbf{x}, \mathbf{s}, \boldsymbol{\omega})$ into a set of mesoscale modes $\{\Psi_i\}$ and spatial-random coupled modes $\{\boldsymbol{\Phi}_i\}$. The dimensionality of the original stochastic microstructure space can be reduced by truncating the bi-orthogonal KLE (Eq. (27)) to d terms, which capture most of the "energy" of the given samples. The truncated bi-orthogonal KLE is given by Eq. (38).

$$\mathbf{A}(\mathbf{x}, \mathbf{s}, \boldsymbol{\omega}) \approx \bar{\mathbf{A}}(\mathbf{x}, \mathbf{s}) + \sum_{i=1}^{d} \sqrt{\rho_i^{(h)}} \Psi_i^{(h)}(\mathbf{s}) \boldsymbol{\Phi}_i^{(h)}(\mathbf{x}, \boldsymbol{\omega}). \tag{38}$$

The mesoscale modes are known as the eigenvectors of the covariance matrix and only depend on the mesoscale coordinates $\mathbf{s}$. The macroscale modes, on the other hand, couple the random source $\boldsymbol{\omega}$ with spatial coordinates $\mathbf{x}$, and they are still high-dimensional random fields. To further reduce the dimensionality, the spatial-random coupled modes resulting from the bi-orthogonal KL expansion need further decomposition. A conventional strategy is to separate the random variables $\boldsymbol{\omega}$ from the spatial coordinates $\mathbf{x}$ using a polynomial chaos expansion (Eq. (39)),

$$\boldsymbol{\Phi}_i^{(h)}(\mathbf{x}, \boldsymbol{\omega}) = \sum_j \boldsymbol{\gamma}_{ij}^{(h)}(\mathbf{x}) \Upsilon_j^{(h)}(\boldsymbol{\zeta}(\boldsymbol{\omega})), \tag{39}$$

where $\Upsilon_j^{(h)}(\boldsymbol{\zeta}(\boldsymbol{\omega}))$ are orthogonal polynomials of random variables $\boldsymbol{\zeta}(\boldsymbol{\omega})$, which usually follow well-known probability distributions. In the current problem, however, the computation of location-specific coefficients $\boldsymbol{\gamma}_{ij}^{(h)}(\mathbf{x})$ is very complicated as $\boldsymbol{\Phi}_i^{(h)}(\mathbf{x}, \boldsymbol{\omega})$ are random fields in terms of spatial coordinates $\mathbf{x}$ and are known only in the form of N (equal to the number of initial samples) finite number of realizations derived from the

bi-orthogonal KLE. The PCE cannot be applied in a straightforward manner to these macro-random coupled modes.

We hereby, propose two reasonable assumptions to simplify the problem and employ a second-level KLE to decompose the random variables from spatial coordinates. The assumptions are:

- The inherent controlling random variables $\boldsymbol{\omega}$ can be separated from the mesoscale and macroscale coordinates $(\mathbf{s}, \mathbf{x})$, as well as the features of the microstructure (i.e. the randomness is independent of the microstructure features, e.g. texture and grain size have the same random source).
- The macroscale modes, $\{\boldsymbol{\Phi}_i^{(h)}\}$, are independent from each other.

The first assumption is natural since it is the fundamental of the decomposition. The second assumption is a strong assumption for arbitrary stochastic processes, since we only have the weak orthogonality condition between macroscale modes (Eq. (32)). However, it is important for the further decomposition of the spatial modes $\boldsymbol{\Phi}_i(\mathbf{x}, \boldsymbol{\omega})$ and we will see later on in this paper that this assumption leads to accurate results.

Having the above two assumptions, we can next perform a second-level KLE on each macro-random coupled mode $\boldsymbol{\Phi}_i$. Omitting the subscript (h), the i-th macro-mode $\boldsymbol{\Phi}_i(\mathbf{x}, \boldsymbol{\omega}_i)$ can be expanded by

$$\boldsymbol{\Phi}_i(\mathbf{x}, \boldsymbol{\omega}_i) \approx \bar{\boldsymbol{\Phi}}_i(\mathbf{x}) + \sum_{j=1}^{r_i} \sqrt{\lambda_i^j} \psi_i^j(\mathbf{x}) \boldsymbol{\phi}_i^j(\boldsymbol{\omega}_i), \bar{\boldsymbol{\Phi}}_i = \frac{1}{N} \sum_{i=1}^{N} \boldsymbol{\Phi}_i^k, \tag{40}$$

where λ_i^j and ψ_i^j are the j-th eigenvalue and eigenvector, respectively, of the covariance matrix,

$$\tilde{\mathbf{C}}_i = \frac{1}{N-1} \sum_{k=1}^{N} \left(\boldsymbol{\Phi}_i^k - \bar{\boldsymbol{\Phi}}_i\right)^T \left(\boldsymbol{\Phi}_i^k - \bar{\boldsymbol{\Phi}}_i\right), \tag{41}$$

and r_i is the number of largest eigenvalues $\{\lambda_i^j\}_{j=1}^{r_i}$ that capture most of the energy of the samples. $\{\boldsymbol{\phi}_i^j\}_{j=1}^{r_i}$, where $i = 1, \ldots, d$, are the reduced representations of the original multiscale microstructures.

In this way, the macro-random coupled modes $\{\boldsymbol{\Phi}_i\}$ are decomposed into basis functions depending on the macroscale coordinates $\mathbf{x}$ and uncorrelated random variables

$\{\boldsymbol{\phi}_i^j\}$. Note that the dimensionality of the stochastic space is reduced for the second time. The dimensionality of the final reduced random space of microstructures over the macroscale is the sum of the principal dimensions that are preserved for representing macro-random modes:

$$r = \sum_{i=1}^{d} r_i, \tag{42}$$

where d is the truncated dimensionality of the bi-orthogonal KLE (Eq. (38)). The reduced stochastic space can then be constructed and equivalently mapped to well-known probability distributions through polynomial chaos expansion introduced in the next section.

4. Polynomial Chaos Expansion of Stochastic Reduced-Order Model

After obtaining reduced representations ($\{\boldsymbol{\phi}_i^j\}_{j=1}^{r_i}$, where $i = 1, \ldots, d$) of the multi-scale microstructure samples, we next need to construct the reduced-order space and map it to a probabilistic space from which new samples are easy to draw. Any sample generated in the low-dimensional surrogate space can be recovered to spatial modes $\boldsymbol{\Phi}$ through Eq. (40) and further reconstructed to a new multiscale microstructure realization in the original input space. Polynomial chaos expansion [9, 29, 30] is therefore introduced to represent $\boldsymbol{\phi}_i^j$ as a function of Gaussian or uniform random variables $\boldsymbol{\zeta}$. As mentioned before, components of $\{\boldsymbol{\phi}_i^j\}_{j=1}^{r_i}$ are uncorrelated but not necessarily independent. Although Rosenblatt transformation [31] can be used to decompose the problem to a set of independent random variables, this is computationally expensive, especially for high-dimensional problems. In this work, we assume the independence between the components of $\{\boldsymbol{\phi}_i^j\}_{j=1}^{r_i}$. It has been shown in various applications [32, 33, 28, 16] that this assumption gives rather accurate results.

Following the independence assumption of $\boldsymbol{\phi}_i^j$, each of them can be expanded on to an one-dimensional polynomial chaos (PC) basis of degree p:

$$\boldsymbol{\phi}_i^j(\omega_i^j) = \sum_{k=0}^{p} \boldsymbol{\gamma}_i^{jk} \Upsilon_i^k(\zeta_i^j(\omega_i^j)), \quad j = 1, \ldots, r_i, \tag{43}$$

where the ζ_i^j are i.i.d. random variables. The random basis functions $\{\Upsilon_i^k\}_{k=0}^{p}$ are chosen according to the type of random variable ζ_i^j that has been used to describe the random

input. For example, if Gaussian random variables are chosen then the Askey based orthogonal polynomials $\{\Upsilon_i^k\}$ are chosen to be Hermite polynomials; if ζ_i^j are chosen to be uniform random variables, then $\{\Upsilon_i^k\}$ must be Legendre polynomials [29].

Uniform-Legendre format is taken for the projection of the reduced-order random variables as it lends very close reconstruction of the PDFs of reduced variables $\boldsymbol{\phi}_i^j$ (see Section 6). The PC coefficients are computed by

$$\boldsymbol{\gamma}_i^{jk} = \frac{E\left[\boldsymbol{\phi}_i^j \Upsilon_i^k(\zeta_i^j)\right]}{E\left[\Upsilon_i^k(\zeta_i^j)\right]}. \tag{44}$$

When Uniform-Legendre is chosen, Eq. (44) becomes

$$\boldsymbol{\gamma}_i^{jk} = \frac{2k+1}{2}\int_{-1}^{1} \boldsymbol{\phi}_i^j \Upsilon_i^k(\zeta_i^j) d\zeta_i^j, \quad j = 1, \ldots, r_i, \quad k = 0, \ldots, p. \tag{45}$$

A proper method is needed to evaluate these integrals. It is noted that the random variable $\boldsymbol{\phi}_i^j$ does not belong to the same stochastic space as ζ_i^j, and we only have N realizations of $\boldsymbol{\phi}_i^j$. The distribution of $\boldsymbol{\phi}_i^j$ is not known. A non-linear mapping $\Gamma : \zeta_i^j \rightarrow \boldsymbol{\phi}_i^j$ is thus needed which preserves properties such that $\Gamma(\zeta_i^j)$ and $\boldsymbol{\phi}_i^j$ have the same distribution. A non-intrusive projection based on empirical cumulative distribution functions (CDFs) of samples developed in [33] is utilized to build the map. The integral in Eq. (45) is then computed using Gauss quadrature.

The non-linear mapping $\Gamma : \zeta \rightarrow \boldsymbol{\phi}$ can be defined as shown below for each $\boldsymbol{\phi}_i^j$:

$$\boldsymbol{\phi}_i^j \stackrel{d}{=} \Gamma_i^j(\zeta_i^j), \quad \Gamma_i^j \equiv F^{-1}_{\boldsymbol{\phi}_i^j} \circ F_{\zeta_i^j}, \tag{46}$$

where $F_{\boldsymbol{\phi}_i^j}$ and $F_{\zeta_i^j}$ denote the CDFs of $\boldsymbol{\phi}_i^j$ and ζ_i^j, respectively. Here, the equalities, "$\stackrel{d}{=}$" is interpreted in the sense of distribution such that the probability density functions (PDFs) of random variables on both sides are equal. The marginal CDF of $\boldsymbol{\phi}_i^j$ samples can be evaluated numerically from the available data. Kernel density estimation is used to construct the empirical CDF of $\boldsymbol{\phi}_i^j$. Let $\{\boldsymbol{\phi}_i^{j,(s)}\}_{s=1}^N$ be the N samples of $\boldsymbol{\phi}_i^j$ obtained from Eq. (40). The marginal PDF of $\boldsymbol{\phi}_i^j$ is then:

$$p_{\boldsymbol{\phi}_i^j}(\boldsymbol{\phi}_i^j) \approx \frac{1}{N}\sum_{s=1}^{N} \frac{1}{\sqrt{2\pi}\tau} \exp\left(-\frac{\boldsymbol{\phi}_i^j - \boldsymbol{\phi}_i^{j,(s)}}{2\tau^2}\right). \tag{47}$$

The marginal CDF of $\boldsymbol{\phi}_i^j$ is obtained by integrating Eq. (47) and the inverse CDF can be computed as well. Having the map Γ_i^j, the coefficients $\boldsymbol{\gamma}_i^{jk}$ are subsequently computed via Gauss quadrature.

After mapping the reduced space to uniform distribution random variables, the Monte Carlo method can be used to sample new microstructure realizations.

5. Problem Definition and Initial Data Set

The problem of interest in this work is the variability of mechanical properties of forged disks due to (initial) microstructure uncertainties. The very first task is to generate initial correlated random microstructures of workpieces to be used as the input to the stochastic simulation. The initial workpiece samples are a set of cylindrical (rectangular in a $2D$ axisymmetric representation) ingots, each point of which is linked to a distinct microstructure (Fig. 3).

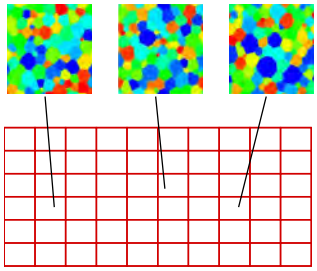

Figure 3: Input to the multiscale deformation simulator.

We generate realizations of the preforms with correlated microstructure using a preprocessing that deforms a set of raw ingots with random surfaces into regular cylinders. The simulations are done within a $2D$ axisymmetric Lagrangian FE framework. The ingots are discretized by 10×6 quadrilateral elements, each of which contains 4 Gauss points for the integration in the element domain. Each Gauss point is linked to a microstructure consisting of 20 grains. One thousand raw ingots whose upper surfaces (Fig. 4) are represented by degree 6 Bezier curves (Eq. (48)) are firstly created.

$$z_\beta(a,\omega) = 0.5 \times \left(1 + \sum_{i=1}^{6} \beta_i(\omega)\varphi_i(a)\right), \tag{48}$$

where

$$\varphi_1(a) = (1-a)^6 + 6a(1-a)^5,$$
$$\varphi_2(a) = 15a^2(1-a)^4,$$
$$\varphi_3(a) = 20a^3(1-a)^3,$$
$$\varphi_4(a) = 15a^4(1-a)^2,$$
$$\varphi_5(a) = 6a^5(1-a),$$
$$\varphi_6(a) = a^6,$$

where $a = x/L$ is the normalized x-coordinate, $\beta_i(\omega)$ are Bezier coefficients, which are i.i.d. randomly sampled from the uniform distribution $\mathcal{U}(-0.1, 0.1)$. At the beginning, we assume all the microstructures to be identical (same grain sizes and texture). The only difference between ingot samples is the random shape of the upper surface. All raw ingots are then used as an input to a deterministic flat-die forging process, during which, their wavy surfaces are flattened under strain rate $v = 0.01s^{-1}$ (Fig. 4). Since all workpieces go through distinct deformation processes due to their unique surface shapes, the resultant microstructures will vary from point to point and from sample to sample. The resultant microstructures after pre-processing are collected as the database of the following stochastic simulation. They will be adopted to build the reduced-order model. In the next step stochastic simulation, new microstructure samples will be sampled and assigned to a regular-shaped workpiece. The flattened workpieces in the pre-process are abandoned. The information about the generation of the random microstructure samples is totally blind to the following stochastic forging simulation.

Since the crystal plasticity constitutive model adopted here only updates grain orientations while leaving grain size untouched, the uncertainty source of the stochastic simulation is the texture of microstructures, which has been proven to have great effect on the mechanical response and properties of polycrystals [12]. The dimensionality of the input is $n_{el} \times n_{int} \times n_{feature} = 60 \times 4 \times 60 = 14400$, where n_{el} is the number of elements in the macroscale discretization, n_{int} is the number of Gauss points of an element, and $n_{feature}$ is the dimensionality of the random feature that describes a microstructures (20 set of 3-dimensional Rodrigues parameters in here). In what fol-

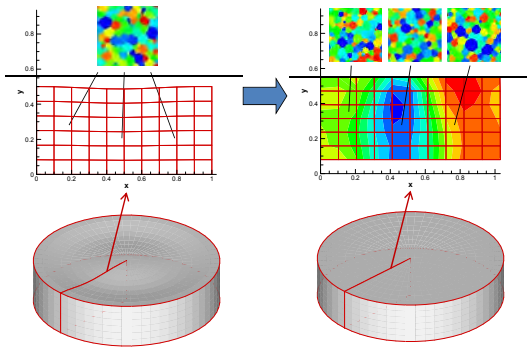

Figure 4: Left: Initial ingot with random upper surface and identical microstructures. Right: Flattened ingot having various resultant microstructures.

lows, the vector $\mathbf{A}(\mathbf{x}, \mathbf{s}, \omega)$ is written as a scalar $A(\mathbf{x}, \mathbf{s}, \omega)$ since the only random source is grain orientation. The number of features that describe a microstructure is therefore being $m = 1$, leading to the fact that $A(\mathbf{x}, \mathbf{s}, \omega)$ is a scalar for a specific $\mathbf{x}$, $\mathbf{s}$ and ω. Consequently, the reduced macroscale modes $\{\Phi_i(\mathbf{x}, \omega)\}_{i=1}^{d}$ and reduced representations $\{\phi_i^j(\omega)\}_{j=1}^{r_i}, i = 1, \ldots, d$ are also scalars for a specific $\mathbf{x}$ and ω. We will adopt the aforementioned two-step KLE to reduce the dimensionality of the stochastic input space driven by the 1000 sets of microstructure samples. The information of how these samples are generated is blind to the model reduction process. The reduced random variables will be mapped to standard multivariate uniform distribution ($\mathcal{U}(-1, 1)$) following the PC expansion through the non-intrusive projection. New samples will be drawn from the reduced space and reconstructed to be the input to the multiscale physical simulator. Monte Carlo simulation is employed to solve the underlying stochastic equations in conjunction with the multiscale deterministic forging solver.

The procedure of the complete uncertainty quantification is illustrated in Fig. 5 and summarized below. (a) to (b): Given a number of initial ingot samples, compute the separated mesoscale and macro-random coupled modes using the bi-orthogonal KLE. (b) to (c): Project the macro-random coupled modes to low-dimensional space through a second-level KLE. (c) to (d) Map the reduced stochastic space to a known (e.g. uniform) distribution using PCE. (d) to (c): Generate new samples in the known low-dimensional distribution, and find their counterparts in the reduced surrogate space

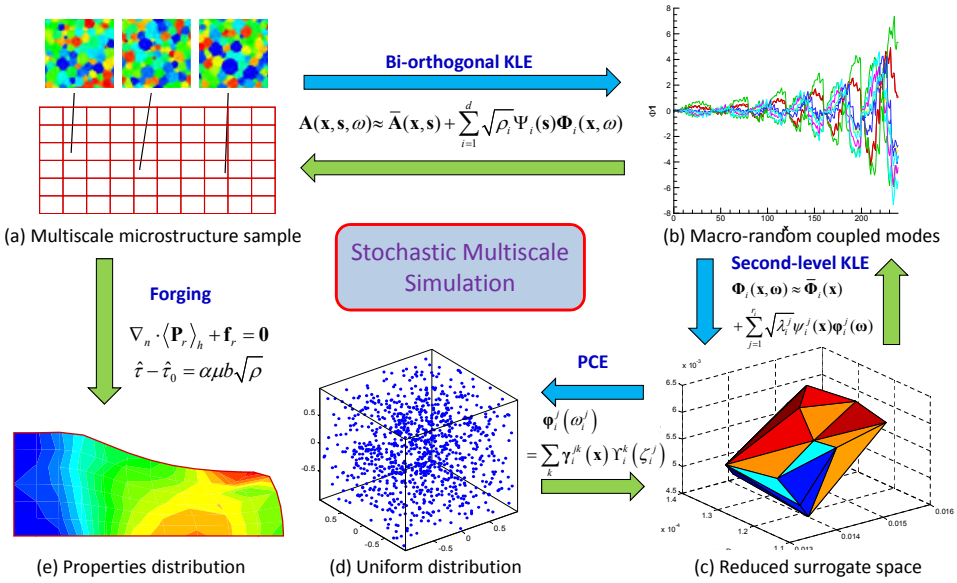

Figure 5: Procedure of the stochastic multiscale simulation for quantifying variability of properties of forging disks due to microstructure uncertainty.

through PCE. (c) to (b) Recover macroscale modes via KLE. (b) to (a): Reconstruct physical representation (microstructures of the workpiece) of new samples using bi-orthogonal KLE after obtaining the macroscale modes. (a) to (e): Perform multiscale forging simulations to obtain the properties of the reconstructed samples. Repeating (d)-(c)-(b)-(a)-(e) multiple times, the statistics of properties of the products can be evaluated.

6. Numerical Examples

We will next validate the bi-orthogonal decomposition strategy for reducing the complexity of stochastic multiscale input. Examples comparing reconstructed features and initial sample features, as well as their corresponding properties after forging, are demonstrated.

6.1. Construction and validation of the reduced-order model

As described in the previous section, 1000 sets of preforms with correlated microstructures (textures) that resulted from the same preprocess are the input to the stochastic simulation. The variability of mechanical properties of the products is induced by the randomness of these initial microstructures. Since each macropoint of the workpiece associates with a 20-grain microstructure, the total dimensionality of the input is 14400 according to the calculation in the previous section. It is impossible to explore such a high dimensional space and investigate the variability of corresponding properties of products. The bi-orthogonal decomposition, followed by a second-level KLE, is applied to the 1000 14400-dimensional samples. We will determine the optimal dimensionality of the reduced space by the proportion of energy captured by the first few principal components.

In bi-orthogonal KLE, the random energy of the k-th macro-random coupled mode is defined by [19]

$$E_k^{(h)}(\omega) := \int_{\mathcal{S}} \rho_k^{(h)} \mathbf{\Phi}_k^{(h)}(\mathbf{x}, \omega) \cdot \mathbf{\Phi}_k^{(h)}(\mathbf{x}, \omega) d\mathbf{x}, \tag{49}$$

The expectation of the random energy is therefore

$$\bar{E}_k^{(h)} = \langle E_k^{(h)} \rangle. \tag{50}$$

Since the mean feature $\bar{\mathbf{A}}$ defined by Eq. (28) has been extracted from the centerized samples $\hat{\mathbf{A}}$, which are the data base of the expansion, the inner product Eq. (30) defined with $h = 0$ should be 0. As a result, $h = 0$ is not appropriate for constructing the covariance matrix and performing model reduction. The covariance matrix when $h = 1$ is identical with the one when $h = 2$, due to Eq. (37). Therefore, we select $h = 1$ as the inner product in the macroscale for the current work.

Computing the energy expectation for all spatial modes, the energy spectrum is plotted in Fig. 6 for $h = 1$. The energy proportion captured by the first d modes is defined as

$$P_{Energy}^{(h)}(d) = \frac{\sum_{i=1}^{d} \bar{E}_i^{(h)}}{\sum_{j=1}^{M} \bar{E}_j^{(h)}}, \tag{51}$$

where the mean energies are sorted in descending order.

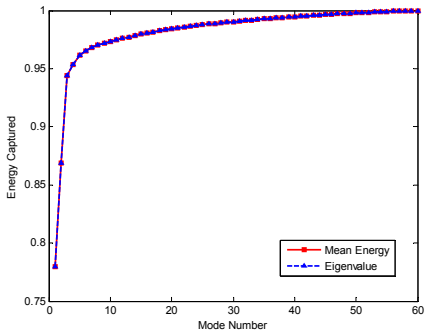

Figure 6: The energy and eigenvalue spectrum of initial samples. The value of y-axis is the total energy proportion captured by the first x principal components.

It is observed that the first few energy components capture most of the total energy. The energy spectrum overlaps with the eigenvalue spectrum defined by

$$P^{(h)}_{Eigenvalue}(d) = \frac{\sum_{i=1}^{d} \rho_i^{(h)}}{\sum_{j=1}^{M} \rho_j^{(h)}}. \tag{52}$$

To effectively reduce the complexity while preserving most of the features of the initial samples, we truncate the bi-orthogonal KLE expansion keeping only the first 3 modes, which captures almost 95% of the total energy. This truncation strategy is similar to that in conventional KLE.

Remark 1: Note that if the mean feature is defined as [19]

$$\bar{\mathbf{A}}(\mathbf{x}) := \frac{1}{|\mathcal{M}|} \int_{\mathcal{M}} \langle \mathbf{A}(\mathbf{x}, \mathbf{s}, \omega) \rangle d\mathbf{s}, \tag{53}$$

the bi-orthogonal decomposition gives different results. In this case the first type of macroscale inner product is not zero any more, and the second type covariance $\mathbf{C}^{(2)}(\mathbf{s}, \acute{\mathbf{s}})$ becomes small. The micro and macro modes become different from the ones presented earlier.

Remark 2: The overlap of the eigenvalue and energy spectrums in Fig. 6 is a result of the current problem setup. Indeed, combining Eqs. (49) and (50), we obtain

$$\bar{E}^{(h)}_k = \int_{\mathcal{S}} \rho_k^{(h)} \left\langle \mathbf{\Phi}_k^{(h)}(\mathbf{x}, \omega) \cdot \mathbf{\Phi}_k^{(h)}(\mathbf{x}, \omega) \right\rangle d\mathbf{x}. \tag{54}$$

When $h = 1$, and considering the orthogonality, we obtain

$$\bar{E}^{(1)}_k = \rho_k^{(1)} \{\mathbf{\Phi}_k^{(1)}, \mathbf{\Phi}_k^{(1)}\}_1 = \rho_k^{(1)}.$$

The energy level of the k-th mode, in general, does not reflect the magnitude of the corresponding eigenvalue. In another words, a mode that possesses large energy does not necessarily correspond to a large eigenvalue. An example is shown in Fig. 7 for the case that $\bar{\mathbf{A}}$ is defined by Eq. (53) and $h = 2$. This outcome is consistent with the results provided in [19]. These facts complicate the performance of the bi-orthogonal decomposition. Therefore, alternative setups (to $h = 1$ and Eq. (28)) are not used in the current work.

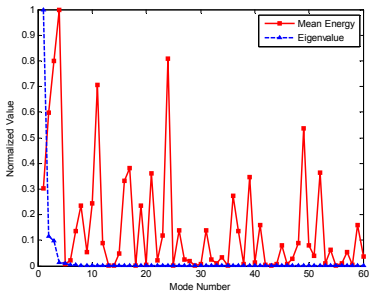

Figure 7: The eigenvalue and mean energy of the bi-orthogonal KLE. Both quantities are normalized with respect to their maximum values.

The reduced spatial modes $\{\Phi_1, \Phi_2, \Phi_3\}$ are presented by 1000 realizations of 240-dimensional vectors, because the mesoscale modes have been segregated. The next task is to separate the random variables from spatial coordinates using a second-level KLE, which results in further reduction of the random space. For each Φ_i ($i = 1, 2, 3$), we perform an independent KLE and keep the largest r_i components that capture more than 95% of the total energy of Φ_i. The energy spectrum of the three modes are plotted in Fig. 8. The number of preserved components are $r_1 = 2, r_2 = 3, r_3 = 3$, respectively. The dimensionality of the final reduced space is therefore $r = r_1 + r_2 + r_3 = 8$.

Remark 3: It is interesting to note that the differences between large eigenvalues and small eigenvalues of the macro-modes Φ_i reduces as i increases. To capture 95% of the total energy, only the largest 2 eigenvalues is enough for Φ_1, while for Φ_2 and Φ_3 three eigenvalues are needed. We also examined the macro-modes that correspond to lower energy in the bi-orthogonal KLE and discovered that 7, 9, 35, and 108 principle components are needed to capture 95% energy of macro modes from Φ_4 to Φ_7, respectively.

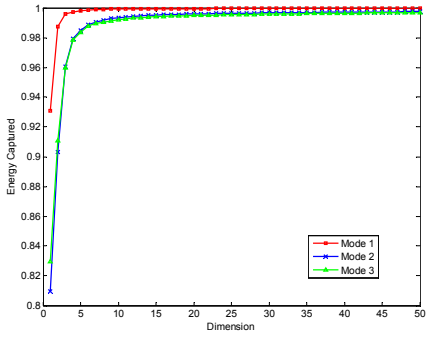

Figure 8: The eigenvalue spectrum of three macro-random coupled modes. The value of y-axis is the total energy proportion captured by the first x principal components. Only the first 50 dimensions are shown.

The increase of the dimensions (e.g. number of principal components) that are necessary to capture the same proportion of the total energy is dramatic, when the energy captured by the macro-modes Φ_i decreases. For this reason, keeping a small number of Φ_i is of great importance to reduce the stochastic space. In the current example, $d = 3$ is the optimal choice.

As we discussed before, the reduced surrogate space of input after two-step KLE needs to be projected to a well-shaped equivalent space through PCE. Therefore, new samples can be easily drawn. Legendre polynomials are selected as we will map the reduced-order random variables to uniform distributions $\mathcal{U}(-1, 1)$. The order of the PC basis is set to be 12, which gives accurate estimation to the distributions of the reduced representations. We plot and compare the PDFs of initial reduced representations and new samples in Figs. 9-11. The distributions of the initial reduced representations $\phi_i^j, i = 1, \ldots, d, j = 1, \ldots, r_i$ are computed from the histogram of the given 1000 initial samples derived by the two-step KLE. On the other hand, 10000 new samples are randomly sampled from the uniform distribution and mapped to the surrogate ϕ_i^j space via PCE. A great consistence of the two curves is observed and thus the PCE on reduced random variables is successful.

To check the performance of the multiscale model reduction, we compare a reconstructed sample with its original realization. An 14400-dimensional array, $\mathbf{A}$, containing the texture information of all initial microstructures over a workpiece realization

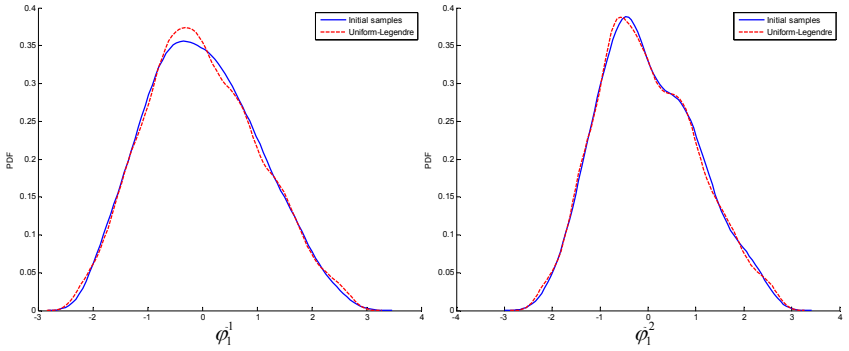

Figure 9: Marginal PDFs of initial low-dimensional representations (i.e. random variables), ϕ_1^j, $j = 1, 2$, corresponding to the first spatial mode Φ_1 (the reduced representations obtained after two-step KLE on the 1000 given texture samples) and identified random variables obtained using PCE (reconstructed through PCE on 10000 randomly generated samples from uniform distribution). The distributions are constructed through kernel density based on data.

is projected to the 8-dimensional uniform distribution through the two-step KLE-PCE process. These 8 reduced variables within $(-1, 1)$ are then mapped back to a 14400-dimensional texture array through the inverse PCE and KLE. We first compare the restored spatial modes from the reduced variables with the initial modes obtained through bi-orthogonal KLE on the original sample. The 3 modes capturing most energy are shown. It is observed in Fig. 12 that the restored $\{\Phi_i\}_{i=1}^3$ are close to the original ones.

We further reconstruct the texture realization in the physical space based on the restored spatial modes through Eq. (38). The restored texture is compared with the original one and a relative error defined as

$$\varepsilon = \frac{1}{M} \sum_{i=1}^{M} \left| \frac{A^i_{Original} - A^i_{Restored}}{A^i_{Original}} \right|, \tag{55}$$

is computed. In Eq. (55), M is the dimensionality of the texture array of the entire workpiece (here, $M = 14400$), $A^i_{Original}$ and $A^i_{Restored}$ are the Rodrigues parameters of the original and restored samples, respectively. Notice that each orientation is described by 3 Rodrigues parameters. In the current setup, we put them all in an 1-dimensional array. Figure 13 (a) shows the reconstructed and original texture of the microstructure associated with one macropoint (for a single microstructure). The relationship between the two samples throughout the entire workpiece is depicted in Fig. 13(b). We observe

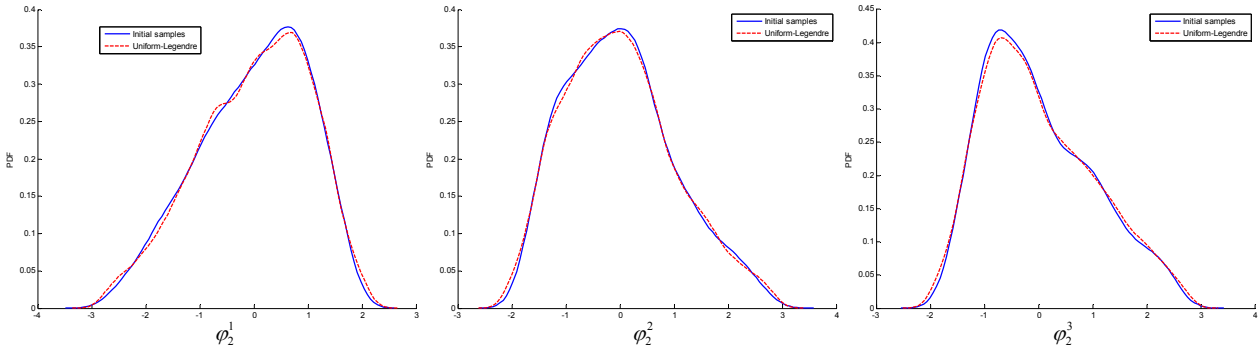

Figure 10: Marginal PDFs of initial low-dimensional representations (i.e. random variables), ϕ_2^j, $j = 1, 2, 3$, corresponding to the second spatial mode Φ_2 (the reduced representations obtained after two-step KLE on the 1000 given texture samples) and identified random variables obtained using PCE (reconstructed through PCE on 10000 randomly generated samples from uniform distribution). The distributions are constructed through kernel density based on data.

a nearly straight line in the original-restored texture plot, meaning that the two samples are almost identical. The deviation of the restored samples from the original one is small. The great consistence of the reconstructed and original samples is obtained. The relative error is $\sim 4.26\%$.

6.2. Stochastic multiscale forging simulation

After establishing the connection between the microstructure space and the reduced surrogate space, we are ready to draw random samples for the investigation of the mechanical properties of workpieces whose microstructures are statistically similar to the given data. The mean and standard deviation of the equivalent strain, stress, and strength fields of the forged workpiece are of interest. The effective strain and stress are evaluated using Eqs. (21) and (22). The effective strength is measured by the average of the slip resistances over all slip systems of all grains in a microstructure (Eq. (24)). The mean and standard deviation fields computed based on 4032 MC samples randomly generated from the reduced-space are plotted in Figs. 14 and 15. The fields computed directly from the 1000 initial samples are also plotted (in the same figures) in comparison with the reconstructed results. The mean fields of properties computed from reconstructed samples are close to the ones computed from the initial samples. This

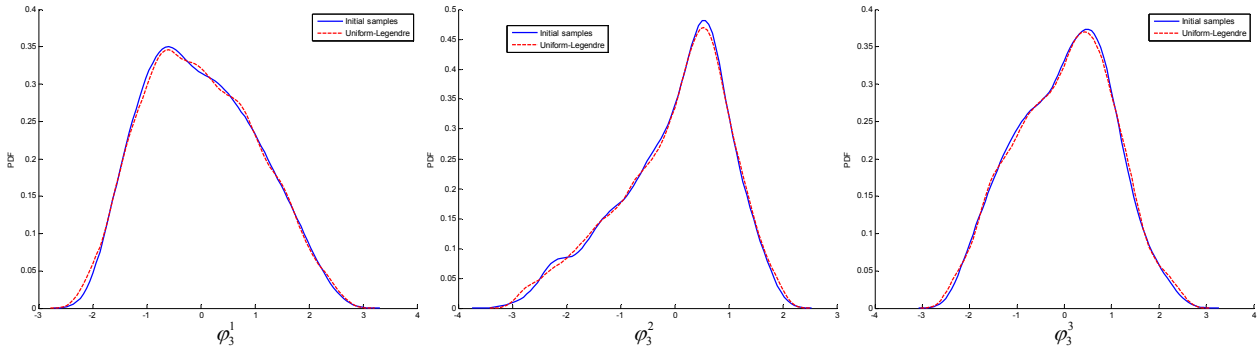

Figure 11: Marginal PDFs of initial low-dimensional representations (i.e. random variables), ϕ_3^j, $j = 1, 2, 3$, corresponding to the third spatial mode Φ_3 (the reduced representations obtained after two-step KLE on the 1000 given texture samples) and identified random variables obtained using PCE (reconstructed through PCE on 10000 randomly generated samples from uniform distribution). The distributions are constructed through kernel density based on data.

is consistent with the bi-orthogonal decomposition setup. The standard deviation of the properties of reconstructed samples, however, shows deviation from that computed using the initial samples. This is because the limited number of given samples are not enough to represent the entire random microstructure space (especially the higher order statistics). On the other hand, the reconstructed samples are generated from the surrogate space which is built to efficiently represent the complete microstructure space. Random samples from the reduced-order model reveal features that cannot be captured by the given initial samples. The gained efficiency in sampling in the low-dimensional surrogate microstructure space is prominent.

A convergence test is also conducted using 8064 random MC samples. The comparison of the mean and standard deviation between 4032 and 8064 samples are plotted in Figs. 16 and 17. The relative difference of quantities between the two sets of simulations defined as $(P_{8064} - P_{4032})/P_{8064}$, where P_N is the quantity evaluated using N MC samples, is plotted in Fig. 18. From the difference we see that the mean fields of the two simulations are almost the same. The relative error of standard deviation fields is larger than that of the mean field. The largest error is around 0.05.

In order to test the convergence of the bi-orthogonal decomposition model reduction scheme, we next keep more components in the second-level KLE so that they

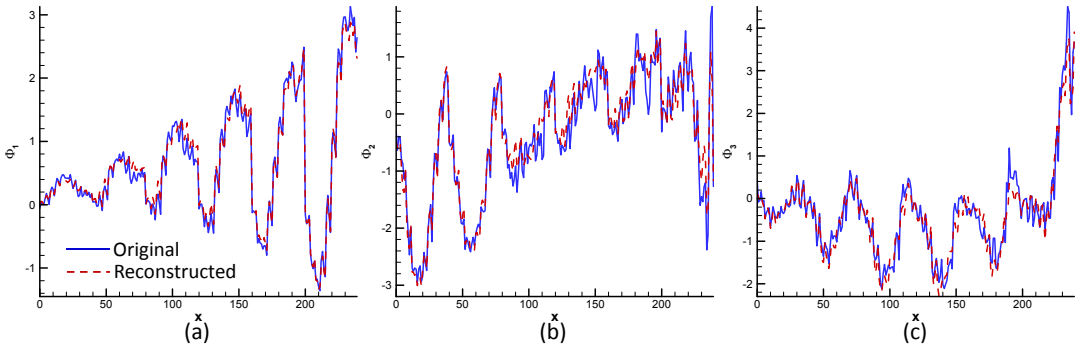

Figure 12: Comparison of reconstructed and initial spatial modes of a single texture sample. The original modes are obtained by projecting a initial texture sample to eigenbasis through bi-orthogonal KLE. The reconstructed modes are recovered from the low-dimensional representations via PCE and second-level KLE. The dimensionality of the reduced representations of Φ_1, Φ_2, and Φ_3 are 2, 3, and 3, respectively.

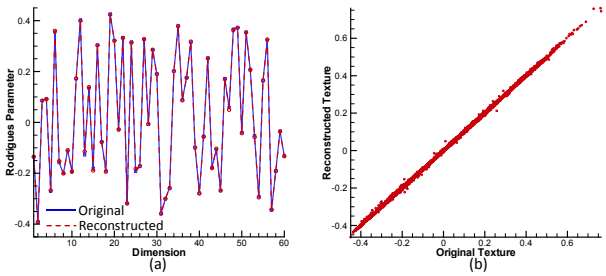

Figure 13: (a) The reconstructed and original texture of the microstructure at a single macropoint. (b) The comparison between the reconstructed texture and its original realization of the entire workpiece. The reconstructed texture is obtained from a 8-dimensional representation.

capture 99% energy of the macro-modes. The dimensionality of the reduced space becomes $r = r_1 + r_2 + r_3 = 3 + 7 + 8 = 18$. The reconstructed macro-modes are obviously closer to their original samples as shown in Fig. 19. Similarly, the reconstructed texture has smaller error, $\varepsilon = 0.0398$, comparing with the original sample (Fig. 20).

The mean and standard deviation of effective strain, stress and strength fields are plotted in Fig. 21. The relative difference of fields defined as $(P_{18} - P_8)/P_{18}$, where P_d is the quantity evaluated from d-dimensional reduced space, is shown in Fig. 22. It is observed that keeping 18 reduced variables gives very similar results as keeping 8 low-dimensional representations, since the total energy captured by the two cases is

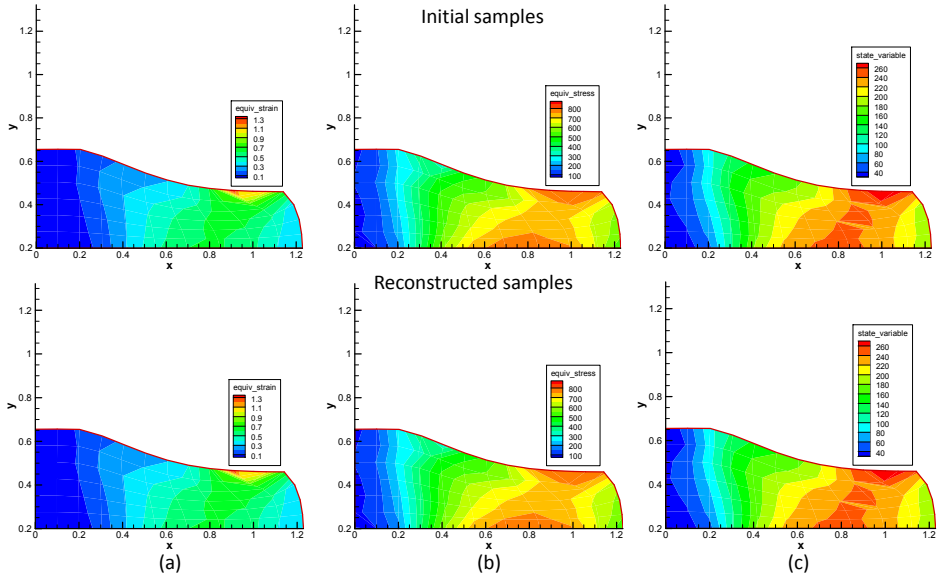

Figure 14: Mean field of the properties of the forged product. Upper: results extracted from 1000 initial samples; lower: results evaluated through 4032 MC samples randomly generated from the 8-dimensional reduced space. (a) effective strain, (b) effective stress, (c) effective strength.

close. The number of samples used here is 8064.

The distributions of properties of any point on the solid can also be computed. In Fig. 23, we plot the equivalent strain, stress, and strength distributions, as well as the convex hull of these three quantities, at a single spot of the workpiece, where the equivalent strain is large. All distributions and the convex hull [34] are evaluated according to the results of 4032 randomly generated samples from the 8-dimensional reduced space in the MC simulation just discussed.

7. Conclusions

A multiscale model reduction scheme based on the bi-orthogonal KLE, conventional KLE and PCE was presented. The basic idea is to decompose the multiscale random field into a few orthogonal modes in different (macro and meso) scales and separate the inherent random variable from the two scale coordinates. A non-intrusive projection strategy is employed to map the reduced representations after the two-step

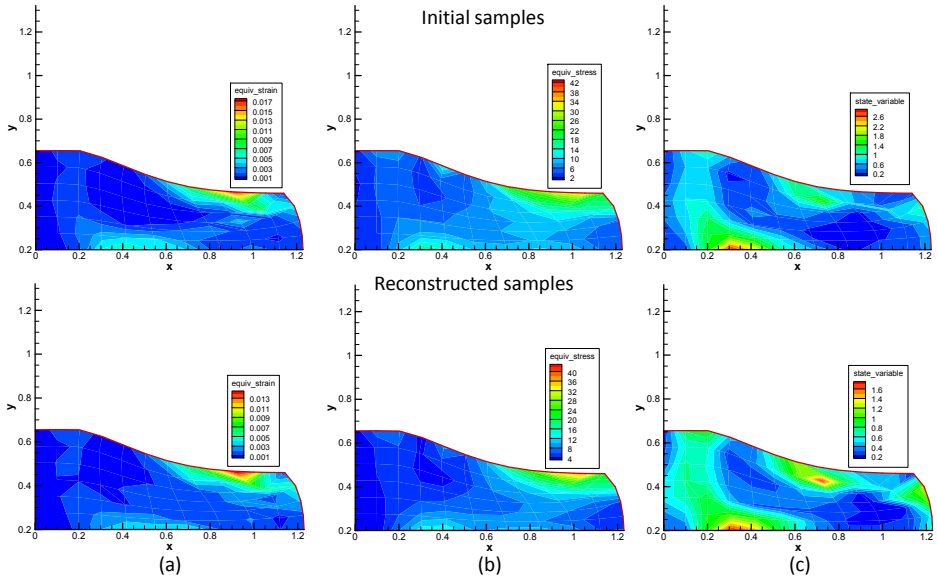

Figure 15: Standard deviation field of the properties of the forged product. Upper: results extracted from 1000 initial samples; lower: results evaluated through 4032 MC samples randomly generated from the 8-dimensional reduced space. (a) effective strain, (b) effective stress, (c) effective strength.

KLE to a multivariate uniform distribution. The reconstructed realizations show agreement with the initial microstructure samples that are given as the known information.

In the context of polycrystalline processes, the multiscale random field is location-dependent high-dimensional random microstructure features, which is reduced to a low-dimensional surrogate space. By sampling in the reduced surrogate space, we can equivalently exploit the original high-dimensional microstructure space. Properties of a continuum workpiece subjected to forging are evaluated by a multiscale solver which couples FE large deformation simulator with crystal plasticity constitutive model. The mean and standard deviation of the equivalent strain, stress, and strength of the final product are computed using MC and ASGC methods. It is seen that the reduced model captures most features of the full model making feasible to perform large scale stochastic multiscale simulation. Future studies will focus on the model reduction of realistic microstructures described by pixels rather than statistical features as in the present work. Moreover, a more robust strategy of decomposing macro-random modes

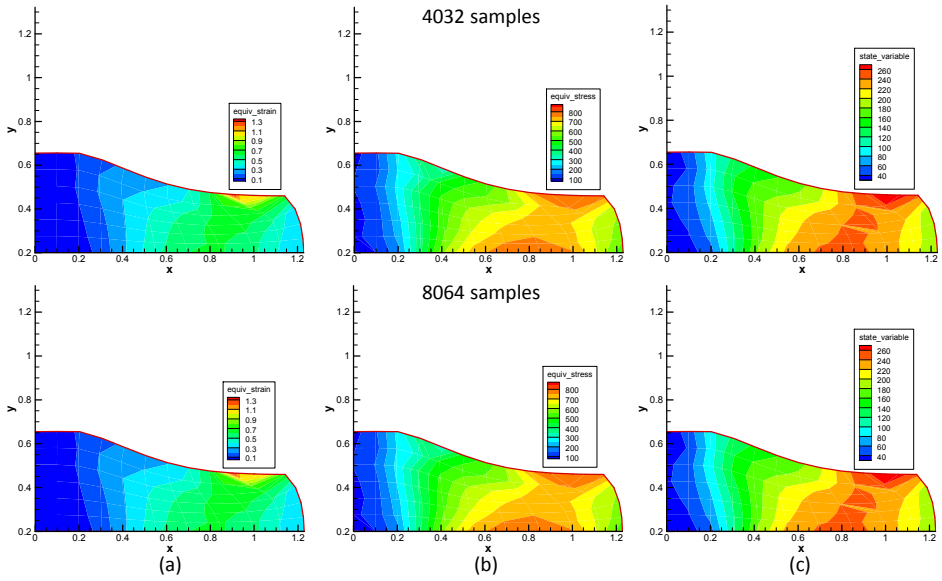

Figure 16: Convergence test of the mean field of the properties of the forged product. Upper: results extracted from 4032 MC samples randomly generated from the 8-dimensional reduced space; lower: results evaluated through 8064 MC samples randomly generated from the 8-dimensional reduced space. (a) effective strain, (b) effective stress, (c) effective strength.

after bi-orthogonal KLE is of interest.

Acknowledgements

This research was supported by an OSD/AFOSR MURI09 award on uncertainty quantification, the U.S. Department of Energy, Office of Science, Advanced Scientific Computing Research and the the Materials Design and Surface Engineering program of the NSF (award CMMI-0757824). This research used resources of the National Energy Research Scientific Computing Center, which is supported by the Office of Science of the U.S. Department of Energy under Contract No. DE-AC02-05CH11231. Additional computing resources were provided by the NSF through TeraGrid resources provided by NCSA under grant number TG-DMS090007.

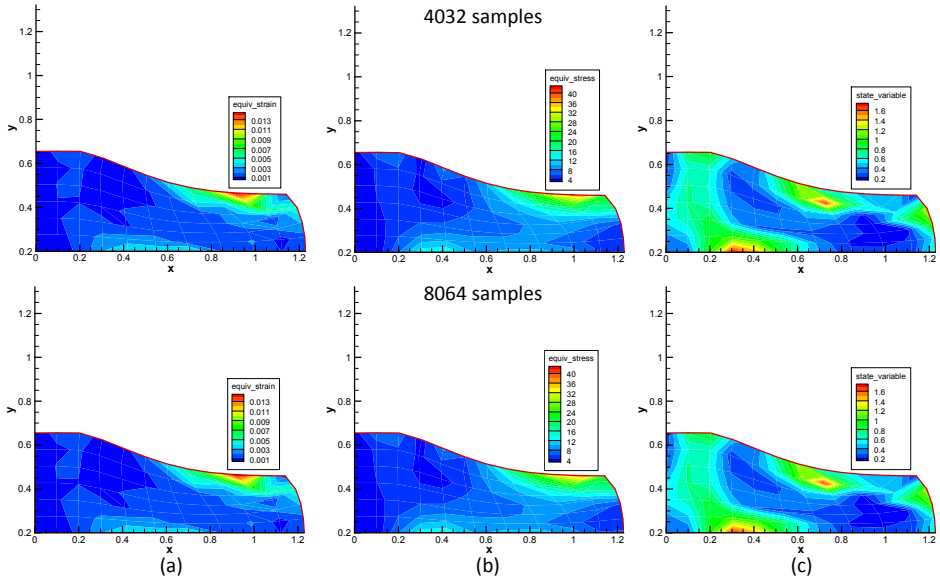

Figure 17: Convergence test of the standard deviation field of the properties of the forged product. Upper: results extracted from 4032 MC samples randomly generated from the 8-dimensional reduced space; lower: results evaluated through 8064 MC samples randomly generated from the 8-dimensional reduced space. (a) effective strain, (b) effective stress, (c) effective strength.

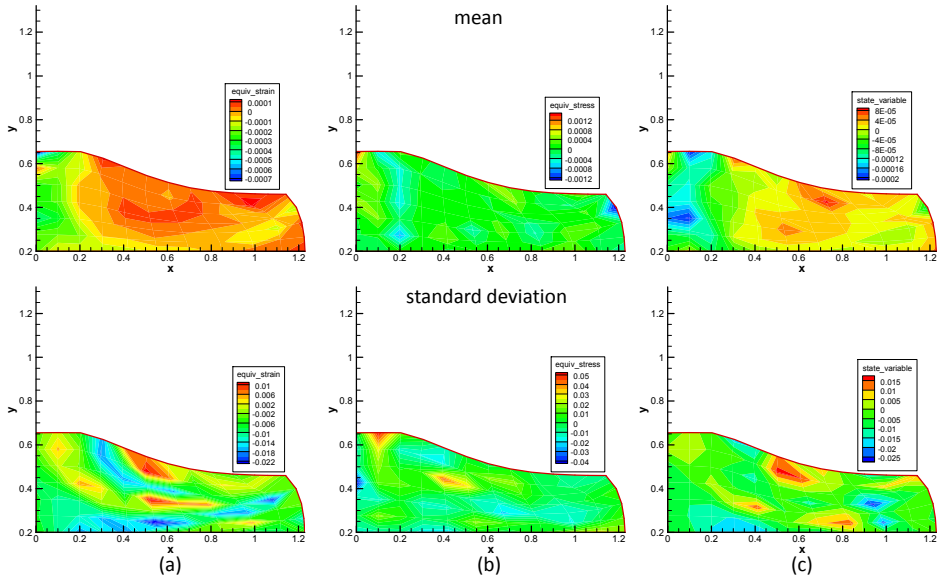

Figure 18: Relative difference of the mean and standard deviation field of the properties of the forged product computed by 8064 and 4032 MC samples drawn from the 8-dimensional reduced space. Upper: difference of mean fields; lower: difference of standard deviation fields. (a) effective strain, (b) effective stress, (c) effective strength.

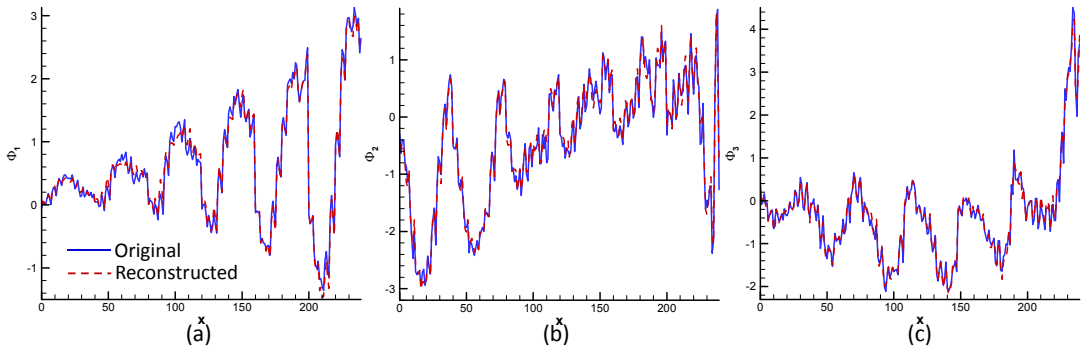

Figure 19: Comparison of reconstructed and initial spatial modes of a single texture sample. The original modes are obtained by projecting a initial texture sample to eigenbasis through bi-orthogonal KLE. The reconstructed modes are recovered from the low-dimensional representations, with higher dimensions, via PCE and second-level KLE. The dimensionality of the reduced representations of Φ_1, Φ_2, and Φ_3 are 3, 7, and 8, respectively.

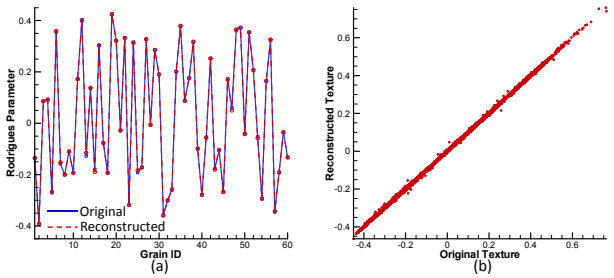

Figure 20: (a) The reconstructed and original texture of the microstructure at a single macropoint. (b) The comparison between the reconstructed texture and its original realization of the entire workpiece. The reconstructed texture is obtained from a 18-dimensional representation.

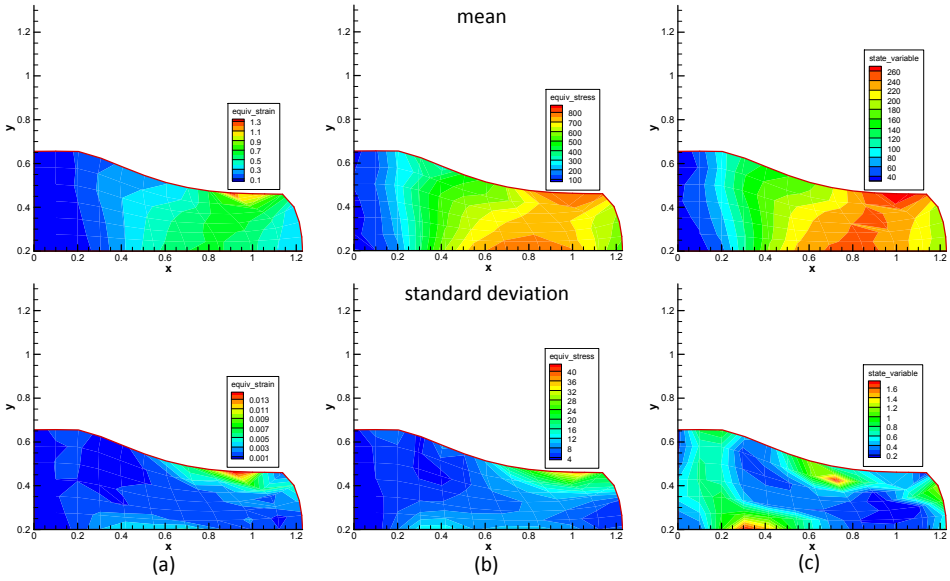

Figure 21: The mean and standard deviation fields of effective strain, stress, and strength computed based on random microstructures reconstructed from 18-dimensional reduced-order representations.

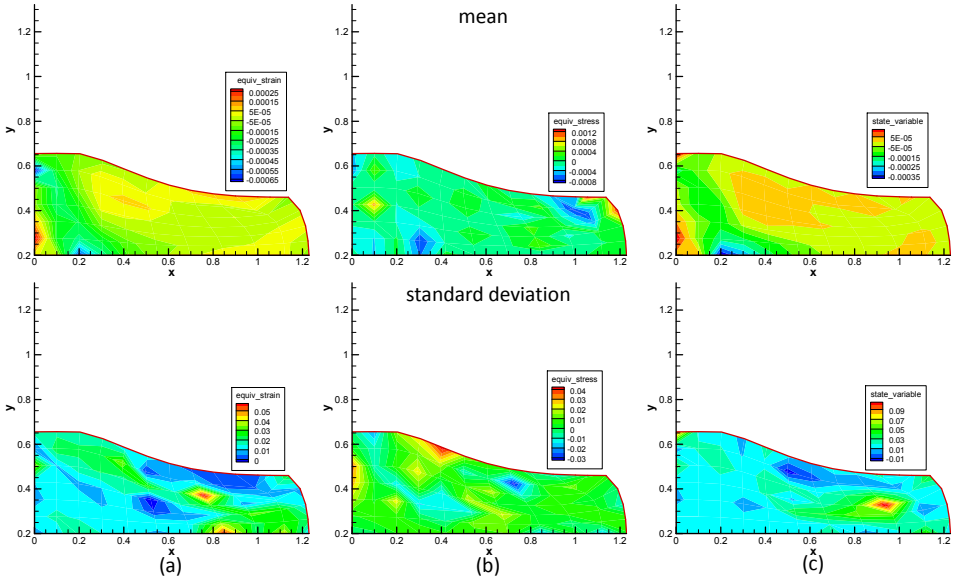

Figure 22: The relative error of mean and standard deviation fields of effective strain, stress, and strength computed based on random microstructures reconstructed from 8-dimensional and 18-dimensional reduced-order representations.

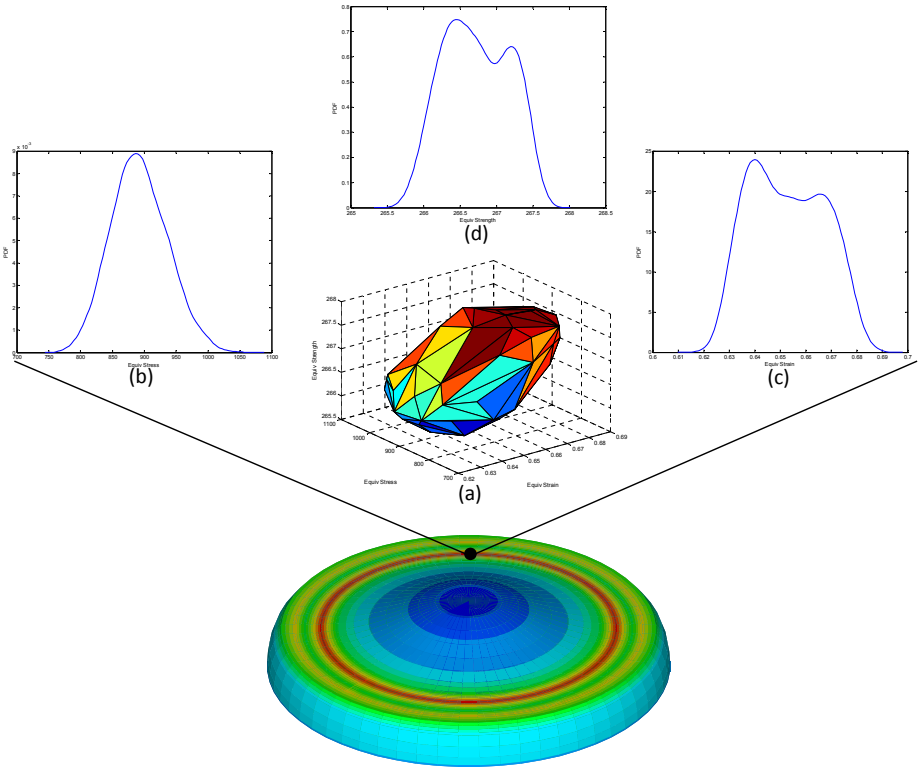

Figure 23: Variability of properties at one single point of the forged disk with random microstructures. (a) A convex hull showing the envelope of the three properties. (b) Equivalent stress distribution. (c) Equivalent strength distribution. (d) Equivalent strain distribution.

References

[1] S. Swaminathan, S. Ghosh, N. J. Pagano, Statistically equivalent representative volume elements for unidirectional composite microstructures: Part i - without damage, Journal of Composite Materials 40 (7) (2006) 583–604.

[2] V. Sundararaghavan, N. Zabaras, Design of microstructure-sensitive properties in elasto-viscoplastic polycrystals using multi-scale homogenization, International Journal of Plasticity 22 (10) (2006) 1799 – 1824.

[3] M. Ostoja-Starzewski, Material spatial randomness: From statistical to representative volume element, Probabilistic Engineering Mechanics 21 (2) (2006) 112 – 132.

[4] S. Sankaran, N. Zabaras, A maximum entropy approach for property prediction of random microstructures, Acta Materialia 54 (8) (2006) 2265 – 2276.

[5] S. Sankaran, N. Zabaras, Computing property variability of polycrystals induced by grain size and orientation uncertainties, Acta Materialia 55 (7) (2007) 2279 – 2290.

[6] L. Anand, M. Kothari, A computational procedure for rate-independent crystal plasticity, Journal of the Mechanics and Physics of Solids 44 (4) (1996) 525 – 558.

[7] B. Kouchmeshky, N. Zabaras, The effect of multiple sources of uncertainty on the convex hull of material properties of polycrystals, Computational Materials Science 47 (2) (2009) 342 – 352.

[8] M. Loève, Probability Theory, fourth ed., Berlin: Springer-Verlag, 1977.

[9] R. Ghanem, P. D. Spanos, Stochastic Finite Elements: A Spectral Approach, Springer - Verlag, New York, 1991.

[10] B. Ganapathysubramanian, N. Zabaras, Sparse grid collocation schemes for stochastic natural convection problems, Journal of Computational Physics 225 (2007) 652 – 685.

[11] X. Ma, N. Zabaras, An adaptive hierarchical sparse grid collocation algorithm for the solution of stochastic differential equations, Journal of Computational Physics 228 (2009) 3084 – 3113.

[12] Z. Li, B. Wen, N. Zabaras, Computing mechanical response variability of polycrystalline microstructures through dimensionality reduction techniques, Computational Materials Science 49 (3) (2010) 568 – 581.

[13] B. Wen, N. Zabaras, Thermal response variability of random polycrystalline microstructures, Communications in Computational Physics 10 (2011) 607–634.

[14] B. Ganapathysubramanian, N. Zabaras, A non-linear dimension reduction methodology for generating data-driven stochastic input models, Journal of Computational Physics 227 (2008) 6612 – 6637.

[15] M. Shenoy, J. Zhang, D. McDowell, Estimating fatigue sensitivity to polycrystalline ni-base superalloy microstructures using a computational approach, Fatigue & Fracture of Engineering Materials & Structures 30 (10) (2007) 889–904.

[16] B. Wen, N. Zabaras, Investigating variability of fatigue indicator parameters of two-phase nickel-based superalloy microstructures, Computational Materials Science 51 (1) (2012) 455 – 481.

[17] T. P. G. J. Gayda, P. T. Kantzos, The effect of dual microstructure heat treatment on an advanced Nickel-base disk alloy, in: Superalloys 2004, TMS, Warrendale, PA, pp. 323–329.

[18] N. Aubry, R. Guyonnet, R. Lima, Spatiotemporal analysis of complex signals: Theory and applications, Journal of Statistical Physics 64 (1991) 683–739.

[19] D. Venturi, X. Wan, G. E. Karniadakis, Stochastic low-dimensional modelling of a random laminar wake past a circular cylinder, Journal of Fluid Mechanics 606 (2008) 339–367.

[20] B. Kouchmeshky, N. Zabaras, Microstructure model reduction and uncertainty quantification in multiscale deformation processes, Computational Materials Science 48 (2) (2010) 213 – 227.

[21] C. Miehe, J. Schröder, J. Schotte, Computational homogenization analysis in finite plasticity simulation of texture development in polycrystalline materials, Computer Methods in Applied Mechanics and Engineering 171 (3-4) (1999) 387 – 418.

[22] A. Acharya, A. J. Beaudoin, Grain-size effect in viscoplastic polycrystals at moderate strains, Journal of the Mechanics and Physics of Solids 48 (10) (2000) 2213 – 2230.

[23] W. Li, N. Zabaras, A virtual environment for the interrogation of 3d polycrystalline microstructures including grain size effects, Computational Materials Science 44 (4) (2009) 1163 – 1177.

[24] U. Kocks, H. Mecking, Physics and phenomenology of strain hardening: the FCC case, Progress in Materials Science 48 (3) (2003) 171–273.

[25] F. Frank, Orientation mapping, Metallurgical and Materials Transactions A 19 (1988) 403–408.

[26] S. Acharjee, N. Zabaras, A concurrent model reduction approach on spatial and random domains for the solution of stochastic PDEs, International Journal for Numerical Methods in Engineering 66 (12) (2006) 1934–1954.

[27] B. Ganapathysubramanian, N. Zabaras, Modeling diffusion in random heterogeneous media: Data-driven models, stochastic collocation and the variational multiscale method, Journal of Computational Physics 226 (1) (2007) 326 – 353.

[28] X. Ma, N. Zabaras, Kernel principal component analysis for stochastic input model generation, Journal of Computational Physics 230 (19) (2011) 7311 – 7331.

[29] D. Xiu, G. E. Karniadakis, The Wiener–Askey Polynomial Chaos for stochastic differential equations, SIAM Journal on Scientific Computing 24 (2002) 619–644.

[30] D. Xiu, G. E. Karniadakis, Modeling uncertainty in flow simulations via generalized polynomial chaos, Journal of Computational Physics 187 (2003) 137 – 167.

[31] M. Rosenblatt, Remarks on a multivariate transformation, Ann. Math. Statist. 23 (1952) 470 – 472.

[32] R. G. Ghanem, A. Doostan, On the construction and analysis of stochastic models: Characterization and propagation of the errors associated with limited data, Journal of Computational Physics 217 (2006) 63 – 81.

[33] G. Stefanou, A. Nouy, A. Clement, Identification of random shapes from images through polynomial chaos expansion of random level set functions, International Journal for Numerical Methods in Engineering 79 (2009) 127 – 155.

[34] C. B. Barber, D. P. Dobkin, H. Huhdanpaa, The quickhull algorithm for convex hulls, ACM Transactions on Mathematical Software 22 (4) (1996) 469–483.